Neutral lipids regulate amphipathic helix affinity for model lipid droplets

Aymeric Chorlay, Abdou Rachid Thiam

JCB Journal of Cell Biology

ARTICLE

Neutral lipids regulate amphipathic helix affinity for model lipid droplets

Aymeric Chorlay and Abdou Rachid Thiam

Cellular lipid droplets (LDs) have a neutral lipid core shielded from the aqueous environment by a phospholipid monolayer containing proteins. These proteins define the biological functions of LDs, and most of them bear amphipathic helices (AH), which can selectively target to LDs, or to LD subsets. How such binding preference happens remains poorly understood. Here, we found that artificial LDs made of different neutral lipids but presenting equal phospholipid packing densities differentially recruit AHs. Varying the phospholipid density shifts the binding levels, but the differential recruitment is unchanged. We found that the binding level of AHs is defined by their interaction preference with neutral lipids and ability to decrease surface tension. The phospholipid packing level regulates mainly the amount of neutral lipid accessible. Therefore, it is the hydrophobic nature of the phospholipid packing voids that controls the binding level of AHs. Our data bring us a major step closer to understanding the binding selectivity of AHs to lipid membranes.

Introduction

Lipid droplets (LDs) are intracellular oil-in-water emulsion droplets, present in almost all organisms and playing diverse biological functions (Olzmann and Carvalho, 2019; Thiam and Beller, 2017; Welte, 2015). They primarily function to maintain cellular energy balance (Walther and Farese, 2012) but are also implicated in several other mechanisms such as protein quality control or lipid stress response (Bersuker and Olzmann, 2017; Shyu et al., 2018). The oil core of LDs is made of neutral lipids whose composition varies between cell types and metabolic conditions (Walther and Farese, 2012). Triacylglycerols and sterol esters (SEs) are the most abundant neutral lipids stored in LDs, but other neutral lipids can be found. For instance, retinol esters, a storage form of vitamin A, are abundant in liver hepatic stellate cells (Blaner et al., 2009); acylceramides, storage forms of ceramides, are made in liver cells under high-fat diet conditions (Senkal et al., 2017); squalene (SQ) or wax oils are also present in many cell types, e.g., skin or plant cells (Spanova and Daum, 2011).

Most neutral lipids are fabricated at the ER bilayer and encapsulated within the bilayer leaflets. When their concentration reaches a threshold, they condense into spherical LDs, which further emerge in the cytosol (Chorlay et al., 2019; Henne et al., 2018; Thiam and Forêt, 2016; Walther et al., 2017). LDs are covered by a single phospholipid (PL) monolayer embedded with proteins, which determine most LD biological functions (Kory et al., 2016). Many of these proteins bind to LDs by using amphipathic helix (AH) domains, motifs that are also capable of targeting bilayer membranes (Bigay and Antonny, 2012; Kory et al., 2016; Thiam and Dugail, 2019). However, despite the fact that bilayer surfaces are much more abundant in cells, many AH-containing proteins achieve to selectively target to the monolayer surface of LDs. Even within a single cell, proteins containing different AHs can preferentially bind to LD subsets, for example made of different neutral lipids (Hsieh et al., 2012; Straub et al., 2008; Thiam and Beller, 2017; Wolins et al., 2006). This occurs for instance with Perilipins (1–5), major LD proteins that bear AH motifs and can preferentially localize to triglyceride or cholesterol ester LDs (Hsieh et al., 2012; Straub et al., 2008), or with the lecithin retinol acyl transferase, whose N terminus AH seem to more strongly associate with retinol palmitate than with triolein (TO) droplets (Molenaar et al., 2019).

Decreasing the PL packing density at the monolayer surface of LDs accentuates the contact between hydrophobic and hydrophilic phases, which is favorable for the binding of AHs (Čopič et al., 2018; Prévost et al., 2018; Thiam et al., 2013a). Indeed, AHs are basically surfactants, and their adsorption to hydrophobic–hydrophilic interfaces is favorable for reducing interfacial energies (Thiam and Dugail, 2019). Currently, there is no experimental determination of the PL packing level at the surface of LDs, nor clear understanding of its contribution to the

Laboratoire de Physique de l'Ecole Normale Supérieure, ENS, Université PSL, Centre National de la Recherche Scientifique, Sorbonne Université, Université de Paris, Paris, France.

Correspondence to Abdou Rachid Thiam: thiam@ens.fr.

binding of AHs. In the case of lipid bilayer, the presence of PL packing defects, or voids, favors the binding of many AHs, by proffering access to the hydrophobic acyl chain core of the bilayer (Bigay and Antonny, 2012; Vanni et al., 2014). In the case of LDs, the situation is different in the sense that AHs have to expose their hydrophobic moieties to neutral lipids. Thus, the nature of the interactions between the hydrophobic amino acids of an AH with neutral lipids could be a major driving force for the targeting of AHs to LDs.

Here, we investigate the contribution of PLs and neutral lipids to the binding of AHs to artificial LDs (aLDs). We find that AHs do not equally bind to the oil/water interface of aLDs made of different neutral lipids but present similar PL packing densities. We subsequently unveil that the chemistry of the neutral lipid has a major contribution to the binding of AHs to LDs. The density of the PL monolayer regulates mainly the amount of neutral lipids accessible to the AHs. These findings highlight that the hydrophobic nature of the packing voids within a PL layer is determinant to the recruitment of AHs.

Results

The binding of AHs to model bilayer-connected LDs depends on the neutral lipid composition

We employed the droplet-embedded vesicle (DEV) system, which consists of aLDs embedded within the bilayer leaflets of a giant vesicle (Chorlay and Thiam, 2018), here made of dioleoylphosphatidylcholine, which is referred to as PC (Fig. 1 A). This topology mimics an LD emerging from the ER membrane, with the bilayer behaving as a PL reservoir to the aLD. DEVs were generated with different neutral lipids: SQ, TO, or TO supplemented with ∼25% (wt/wt) SE (TO-SE), which was around the maximum solubility of SE in TO at room temperature.

We first wondered whether the neutral lipid type affects the surface tension of spherical aLDs emerging from the bilayer. By using a microaspiration technique, we measured this tension (Fig. 1 B) and found it respectively of 0.58 mN/m for SQ, 1.63 mN/m for TO, and 1.84 mN/m for TO-SE (Fig. 1 C). These values are comparable to the surface tension of LDs isolated from mammalian or fly cells (Ben M'barek et al., 2017). SQ aLDs had a lower interfacial tension than TO-containing aLDs. Supplementing TO with 25% SE was sufficient to slightly increase surface tension; pure SE-LDs can be expected to have an even higher surface tension. These results suggest that LDs may emerge from the ER bilayer with different interfacial energies with respect to their neutral lipid content. This interfacial energy could be further reduced by the recruitment of amphipathic molecules such as AHs (Chorlay et al., 2019). Thus, we hypothesized that AHs would be differently recruited to the surface of emerging aLDs made of different neutral lipids.

We studied the recruitment of fluorescently labeled AH peptides derived from proteins reported to bind to LDs. Several AHs were considered so as to cover as much as possible diverse amino acid features. We used an NBD-tagged AH sequence from caveolin 1 (Cav aa159–178, termed Cav1-AH) which was used to target hydrophobic peptides to the surface of cellular LDs (Kassan et al., 2013); a rhodamine-tagged AH sequence from Arfgap1, which is a PL packing sensor (Bigay et al., 2005) also found on LDs (Gannon et al., 2014); a short NBD-tagged AH in the 11-mer repeat sequence of Plin1 (Plin1_108-137; Ajjaji et al., 2019; Rowe et al., 2016), which is the major LD protein in adipocytes (Brasaemle, 2007; Fig. S1 C); and finally, a rhodamine-tagged AH of the nonstructural protein 5 of the hepatitis C virus, which binds to LDs during viral replication (Shi et al., 2002). As the larger difference in surface tension was measured between SQ and TO (Fig. 1 C), we focused on the binding of the peptides to aLDs made of these two neutral lipids. This strategy would a priori enable better discrimination of the role of the neutral lipid type in recruitment.

The peptides were added to the external medium of the DEVs (Fig. 1 D). To quantify binding, we defined the "droplet enrichment index," which is the peptide signal on the droplet normalized by the one on the bilayer, corrected by an optical factor (β) that accounts for the optical index mismatch between the oil droplet and the external water phase (Fig. 1 D and Fig. S2). Cav1-AH, Arfgap1-AH, and NS5A-AH were recruited much more to TO than to SQ aLDs (Fig. 1, E–I; and Fig. S1 B), proving that the neutral lipid content impacts the recruitment level of an AH. On the contrary, Plin1_108-137-AH barely bound to TO or SQ aLD (Fig. 1 I and Fig. S1 C), showing the importance of amino acid composition on AH LD binding. Membrane binding is particularly favored by bulky hydrophobic residues (Prévost et al., 2018; Wimley and White, 1993), such as tryptophan or phenylalanine, which are present in Cav1-AH, Arfgap1-AH, and NS5A but not Plin1_108-137-AH (Fig. 1, E and G; and Fig. S1, B and C). NS5A-AH, for instance, bears the larger number of bulky hydrophobic residues and was more strongly recruited to both neutral lipids than other AHs. However, the presence of hydrophobic bulky residues is not mandatory to guarantee stable binding. Indeed, when we mutated the two phenylalanines of Cav1-AH into leucine (F2L,F8L), the binding efficiency onto TO aLDs was similar to that of the wild-type AH (Fig. 1 J and Fig. S1 D). The presence of opposite charges on the hydrophilic face of the AH might have promoted lateral AH–AH interaction and stabilized binding, as proposed for Plin4 (Čopič et al., 2018). On the contrary, when we put a charge in the hydrophobic face of the AH, by mutating the valine into arginine (V5R), we lost binding to the aLDs (Fig. 1 J and Fig. S1 D). Finally, Arf1 protein binds to membranes and to LDs (Guo et al., 2008; Thiam et al., 2013a) with an AH dense in tryptophan and phenylalanine, in combination with a myristoylated acyl chain. In the presence of GTP and EDTA, to activate Arf1 binding (Antonny et al., 1997), the recruitment to TO aLDs was much higher than for other AHs, and much more than to SQ aLDs (Fig. S1 E).

To further validate our observation on the influence of the oil type on peptide recruitment, we used dodecane, which is a nonphysiological oil whose measured oil/buffer interfacial tension (31.8 mN/m) was between SQ and TO (23.7 mN/m and 34.1 mN/m, respectively). We found that both Cav1-AH and Arfgap1-AH were enriched to dodecane aLDs at intermediate levels between SQ and TO (Fig. S1 A).

Altogether, these results indicate that the neutral lipid composition impacts the recruitment level of AHs to aLDs connected to a bilayer. Here, the recruitment of the AHs was more

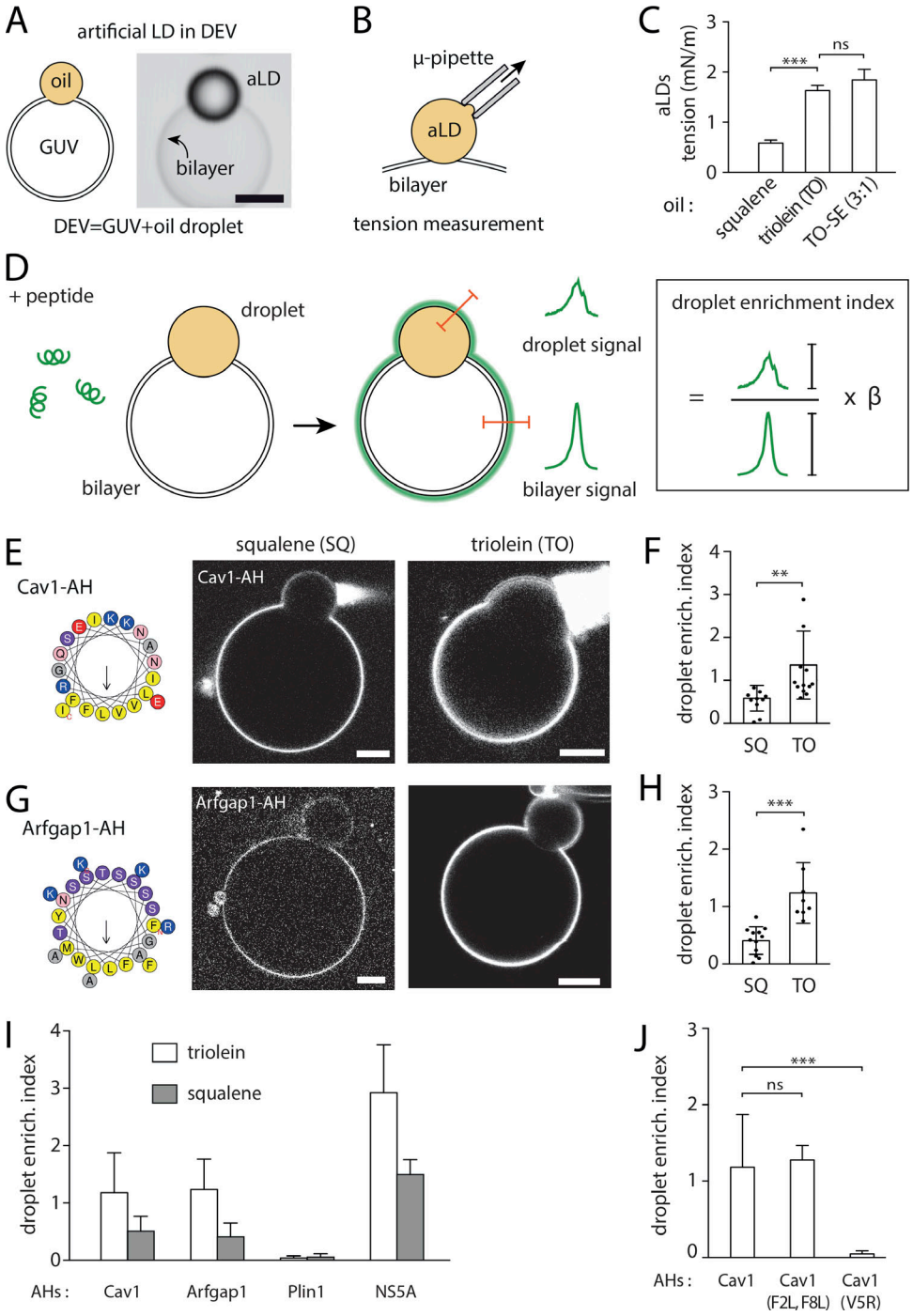

Figure 1. **AHs differentially bind to aLDs emerging from a bilayer and made of different neutral lipids. (A)** Diagram of an aLD incorporated in the inter-monolayer space of a GUV bilayer, forming the DEV system. Example of a DEV is shown on the right. Scale bar, 5 µm. **(B)** Surface tension of an aLD in a DEV is measured using the micropipette aspiration technique. **(C)** Surface tension of aLDs in DEV made using SQ, TO, and TO mixed with 25% of SE. **(D)** A solution of fluorescently tagged peptide is added to a DEV. The peptide is recruited to the DEV interfaces. Fluorescent signal is quantified on the aLD and the GUV bilayer. We calculated a droplet enrichment index by taking the ratio between droplet signal and GUV bilayer signal and multiply it by an optical correction factor (β); see Fig. S2. **(E)** Cav1-AH tagged with NBD is added to a DEV solution. Micrographs show Cav1-AH recruited to DEVs containing SQ or TO aLDs. Scale bars, 10 µm. See also Fig. S1 A. **(F)** Quantification of droplet enrichment index for both SQ and TO aLDs. TO droplets recruited more Cav1-AH as compared with SQ droplets. *t* test shows significant difference ($P < 0.001$). Data are represented as mean ± SD. **(G)** Arfgap1-AH tagged with rhodamine B is added to a DEV solution. Micrographs show Arfgap1-AH recruited to the DEV surface containing SQ or TO aLDs. Scale bars, 10 µm. See also Fig. S1 B. **(H)** Quantification of droplet enrichment index for both SQ and TO aLDs. TO droplets recruited more Arfgap1-AH as compared with SQ droplets. *t* test shows significant difference ($P < 0.0001$). Data are represented as mean ± SD. **(I)** Droplet enrichment index of AH from Caveolin 1 (Cav1), Arfgap1 (Arfgap1), and Perilipin 1 (Plin1). *t* test shows significant differences between TO and SQ with $P < 0.0001$ for all AH tested except for the AH from Perilipin 1. Data are represented as mean ± SD. See also Fig. S1, B, C, and E. **(J)** Droplet enrichment index for Cav1-AH and mutated versions: Cav1-AH(F2L,F8L), two phenylalanines mutated into leucine, Cav1-AH(V5R) by mutating the valine into arginine in the hydrophobic face. *t* test shows no significant difference between Cav1-AH and Cav1-AH(F2L,F8L) ($P = 0.71$) but shows significant differences between Cav1-AH and Cav1-AH(V5R) with $P < 0.0001$. Data are represented as mean ± SD. See also Fig. S1 D.

favorable to TO than SQ aLDs and also depended on the amphipathic sequence.

The PL packing density of the model bilayer-connected LDs is independent of the neutral lipid content

Arfgap1-AH is a PL packing sensor (Bigay et al., 2005) that is better bound to TO than to SQ aLDs (Fig. 1 I). We hence thought that aLDs connected to bilayers might present different PL packing levels according to their neutral lipid content. This would be consistent with the difference in surface tension and AH recruitment between TO and SQ. To quantify the PLs density, we made PC DEVs containing 1% of nickel PL (DGS NTA(Ni)), which covalently binds to histidine. Histidine-mCherry was added to the medium and recruited to DEVs by nickel lipids (Fig. 2 A and Fig. S3 I). The PL density at the aLD and the bilayer interfaces of the DEV was hence reported by mCherry signal.

DEVs were imaged at their lowest plane (Fig. 2 A), which yields a signal not reduced by the index mismatch between the water phase and the oil droplet (Fig. 2 B and Fig. S2). By measuring the aLD mCherry signal normalized to that of the bilayer, we found no significant difference between SQ, TO, and TO-SE (Fig. 2 C and Fig. S3, A and B). The average fluorescence ratio between the aLD and the bilayer was ∼0.87, below 1, suggesting that the PL density of the aLD monolayer was constant and lower than that of the bilayer: on average, for 100 PLs on the monolayer of the bilayer, there are ∼87 PLs on the monolayer of the droplet (Fig. 2 C, bottom). This finding indicates that the differential recruitment of the AHs between SQ and TO aLDs was not due to a difference in PL packing.

It is well known that the PL packing density correlates with the binding of AHs (Bigay et al., 2005; Čopič et al., 2018; Pranke et al., 2011; Prévost et al., 2018), but here it did not seem to explain the differential recruitment of the tested AHs. We thus sought an independent confirmation of this unanticipated finding of the unchanged PL density at the monolayer covering the different neutral lipids. We opted for a droplet tensiometer measurement, which is a complementary and nonfluorescence method, to our previous approach. We generated a neutral lipid-in-buffer droplet whose interface was decorated by PC, which was added from the aqueous phase in the form of liposomes (Fig. 2 D), and we measured the surface tension. We next performed droplet area oscillations by imposing blowing-shrinking cycles of the droplet volume. This manipulation enables to probe the rheology of the monolayer and to extract its elastic modulus (E). This modulus reflects the lateral interactions between PLs and is therefore linked to the PL monolayer density (Fainerman et al., 2002; Kralchevsky et al., 2008). The droplet was next shrunk to increase the PL density and the oscillation repeated, and so on and so forth (Fig. S4). These operations enabled to establish the dependence of the elastic modulus (E) against the monolayer lateral pressure (π; Fig. 2 E), which is directly linked to the area per PL through the isotherm of compression. A subsequent mathematical fitting of this curve by the Frumkin isotherm model (Kolev et al., 2002; Kralchevsky et al., 2008) enabled extraction of the area occupied by a PL at the neutral lipid–buffer interface (Fig. 2 F). For both TO and SQ, the experimental data points and the fitting curve followed a similar trend (Fig. 2 E), suggesting an equivalent PL density at the neutral lipid–buffer surface. At a surface pressure of ∼30 mN/m, corresponding to a surface tension of ∼1 mN/m, which is close to the one of aLDs (Fig. 1 C) and to that of cellular LDs (Ben M'barek et al., 2017), the area per PC lipid at the monolayer interface was found to be ∼78 Å^2 (Fig. 2 G). This area was identical for SQ and TO, and even for the nonphysiological dodecane oil (Fig. S3, C–F), with the precision of the measurement technique. Note that for a bilayer, the surface area of a PC molecule varies between 69.7 Å^2 and 74 Å^2 (Fig. 2 H; Kučerka et al., 2008; Reddy et al., 2012), based on the maximum bilayer area expansion (Fig. S3, G and H); this range of area is indeed slightly smaller than the 78 Å^2 area on the monolayer, and consistent with our previous findings with DEVs (Fig. 2 C).

In conclusion, our data reveal that the density of PC molecules on the monolayer of an aLD connected to a bilayer is independent of the tested neutral lipids and is ∼0.87 times smaller than the density in the bilayer (Fig. 2, C, G, and H).

AHs are differentially recruited to bare neutral lipid/buffer interfaces

Since the PL packing density was identical for SQ and TO aLDs, it did not explain the differential recruitment of the AHs (Fig. 1, E–I). Therefore, it was probably the nature of the interactions between the AH and the neutral lipid interface that was responsible for the differential binding observed in Fig. 1. To test this hypothesis, we produced simultaneously PL-free TO and SQ droplets in buffer (Fig. 3 A). We added Cav1-AH, Arfgap1-AH, or Plin1_108-137-AH to the buffer and measured their fluorescence signal at the surface of the droplets (Fig. 3 B). We observed a neat difference in recruitment: AHs were much more enriched to the TO-buffer than to the SQ-buffer interfaces. Note that the net recruitment was higher for Cav1-AH than for Plin1_108-137-AH (Fig. S5 H), as for the aLDs of DEVs (Fig. 1 I). Here, to appreciate the differential recruitment for each AH, the recruitment signal was normalized by the signal at the TO/buffer interface.

What makes an AH more favorably binding to a given neutral lipid/buffer interface? To provide hints to this question, we decided to map the binding efficiency for a variety of neutral lipid conditions and focused on Cav1-AH and Plin1_108-137, which had contrasted binding efficiencies (Fig. 1 I and Fig. 3 B). We started by mixing SQ and TO at different ratios, as binding of the AHs was highly different between these two neutral lipids. Increasing the SQ fraction decreased the binding of both peptides (Fig. S5 A), even though this decrease was a little bit more pronounced for Cav1-AH. In contrast, while 25% of SQ in TO strongly decreased the relative recruitment of both AHs (Fig. S5 A), the presence of 25% SE in TO did not alter this binding (Fig. 3 C and Fig. S5 B). In TO/diolein mixtures, Cav1-AH recruitment is decreased by diolein presence, while Plin1_108-137-AH recruitment remained intact (Fig. 3 C and Fig. S5 C). We next tested the effect of monoolein addition and, contrarily to diolein, found a strong decrease of binding for both AHs. This is probably because monoolein behaves more like a surfactant, which is recruited and protects the neutral lipid/buffer surface from AH recruitment (Fig. S5 D; Thiam et al., 2013b). We also compared the recruitment to TO and retinol palmitate, a major neutral

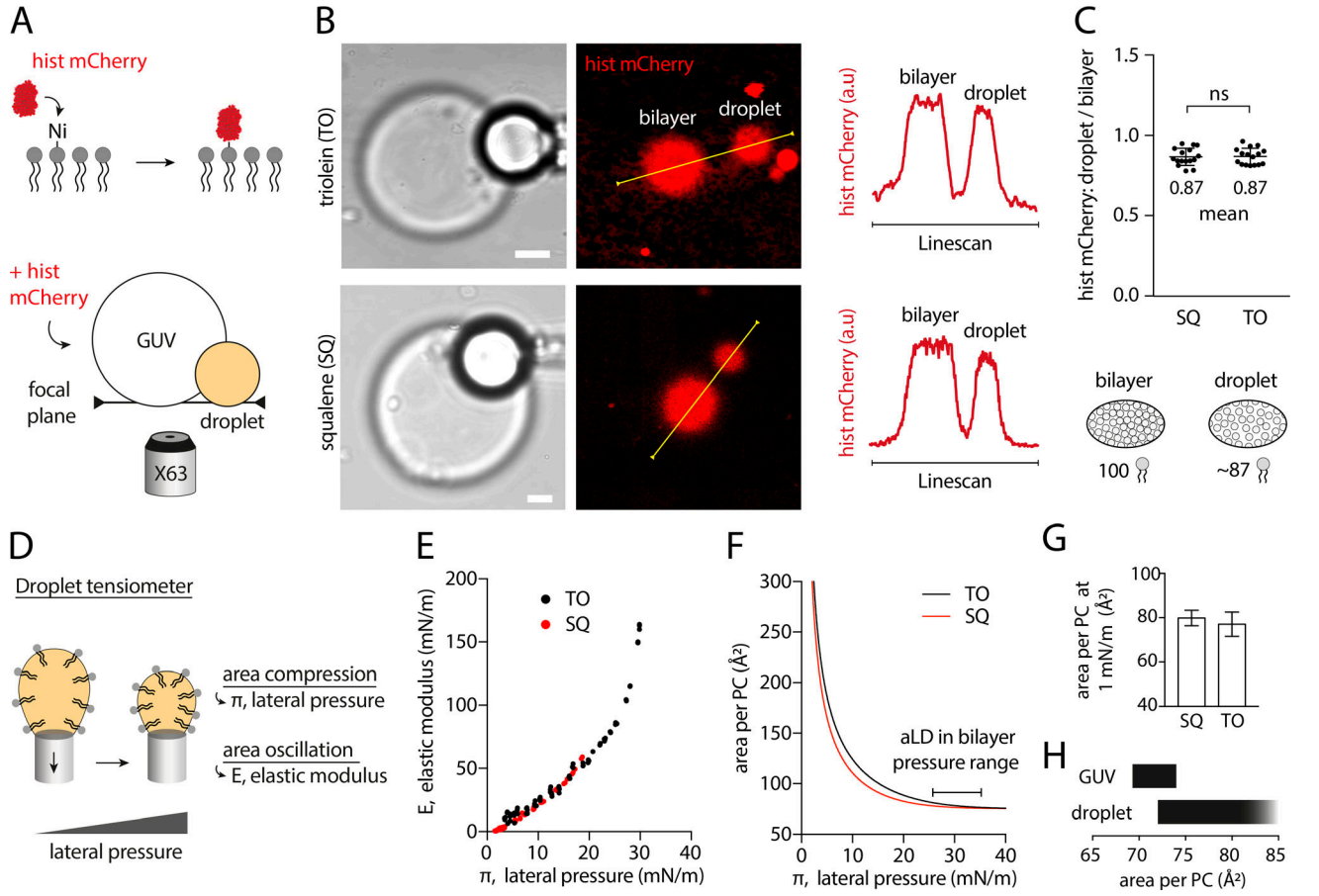

Figure 2. **The PL packing level is identical on aLDs emerging from a bilayer, independently of neutral lipid composition tested. (A)** Schematic diagram illustrating the method for measuring the relative PL density on DEVs. Top: fluorescent mCherry-histidine binds to nickel PLs (DGS-Ni-NTA). Bottom: mCherry-histidine is added to DEV system made with PC presenting 1% nickel PLs. After 10-min incubation with mCherry-histidine, the GUV membrane and aLD surface are visualized simultaneously at their apex (same focal plane). Control experiment without nickel lipid is shown in Fig. S3 I. **(B)** Representative confocal fluorescence images of mCherry-histidine marking PLs of DEV containing SQ or TO aLDs. Linescans allow for the quantification of fluorescence intensity on the GUV membrane and droplet surface. Scale bar, 5 µm. **(C)** Top: Quantification of the ratio between the droplet and bilayer fluorescence intensities for SQ and TO aLDs. *t* test shows no significant difference. Data are represented as mean ± SD. DEVs containing TO-SE aLDs were also imaged and quantified; they show no difference with TO and SQ (see Fig. S3, A and B). Bottom: Cartoon of the PC density on an aLD and a bilayer of a DEV: for an identical area, 100 PC molecules on the bilayer and ∼87 PC molecules on the aLD. **(D)** PC-covered oil droplet surface was characterized by using a droplet tensiometer method. PL lateral pressure (π) is increased by reducing the droplet surface area, and area oscillation enables measurement of the interface elastic modulus (E). **(E)** E-π isotherms for SQ and TO oil phase. **(F)** Area per PC molecule as function of the lateral pressure π at SQ and TO/buffer interface. Data are obtained by fitting the experimental E-π isotherms with a Frumkin theoretical model. Lateral pressure region typically encountered in DEV systems and in cellular LDs corresponds to the flat area around 30 mN/m. **(G)** Area per PC molecule on SQ and TO aLD, at 1 mN/m surface tension; see Fig. S3 E. 1 mN/m was chosen as the average surface tension of aLDs just emerging from a bilayer, and close to the surface tension of cellular LDs. Similar results for dodecane oil are displayed in Fig. S3, C–F. See Fig. S4 for raw data. **(H)** Area variation range of a PC molecule on a bilayer and a droplet monolayer.

lipid in hepatic stellate cell, and found much less recruitment to the latter for both AHs (Fig. 3 C and Fig. S5 E). More generally, we found that even nonphysiological oils were discriminated by these AHs (Fig. S5 F). Altogether, these results highlight two major points: the neutral lipid composition determines the binding level of AHs, and the ability of AHs to discriminate between neutral lipids relies on their amphipathic amino acid sequence. To further illustrate the latter, we thought that the point mutations done on Cav1-AH could be sufficient to alter its propensity to discriminate between SQ and TO. Indeed, we found that the F2L,F8L mutant surprisingly showed slightly more improved distinction between the neutral lipids, while the V5R mutant lost discernment (Fig. 3 D and Fig. S5 G).

The above experiments gave us enough source of variability to analyze for better understanding parameters controlling recruitment. One characteristic of recruitment is the minimization of interfacial energies. For example, bare TO/buffer surface tension was 34.1 mN/m, which is much higher than that of SQ/buffer, which was 23.7 mN/m. This higher tension for the TO interface could have favored the higher recruitment of the AHs, because of the higher energy cost for exposing TO than SQ to water molecules. Therefore, one predicts that surface tension correlates with recruitment. Thus, we represented the surface tension of all the tested neutral lipids and nonphysiological oils against the recruitment level of Cav1-AH or Plin1_108-137 (Fig. S5, I and J). For Cav1-AH, we found indeed that binding overall

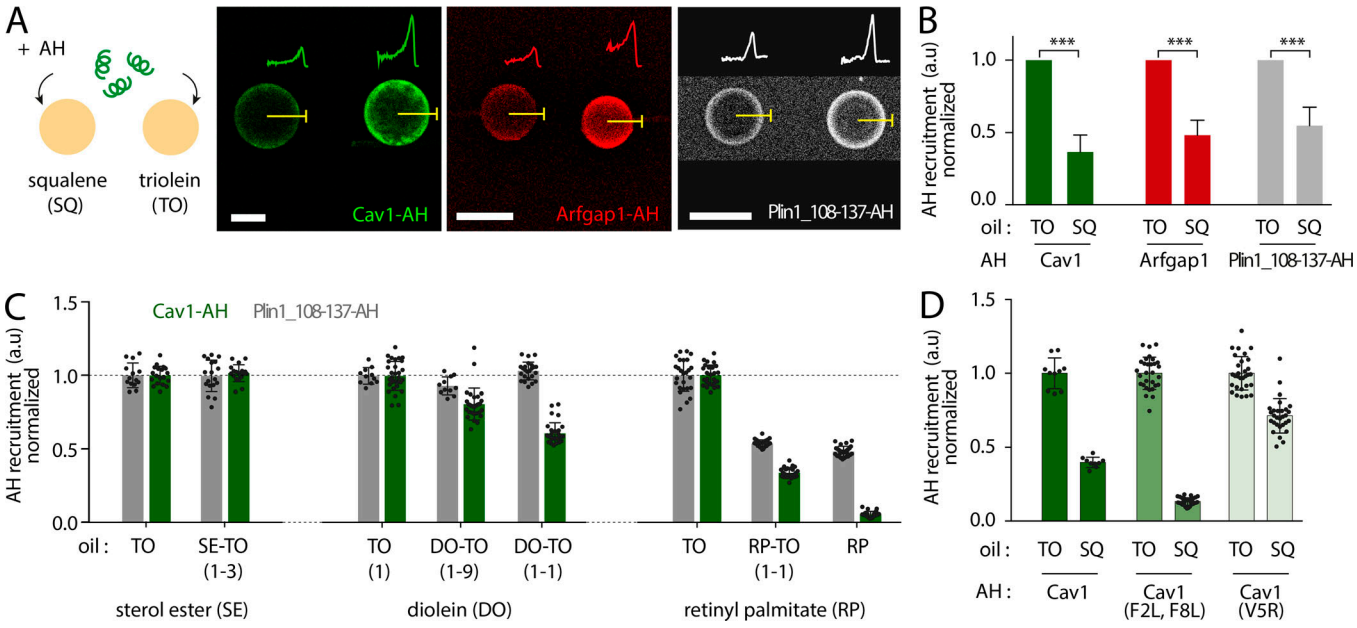

Figure 3. **AHs have differential affinities for neutral lipids. (A)** PL-free SQ and TO droplets are formed in buffer containing AHs (Cav1-AH, Arfgap1-AH, or Plin1_108-137-AH). Left: Representative confocal fluorescence images showing the recruitment level of the AHs are shown. The fluorescent signal is quantified on each droplet. Scale bar, 50 µm. **(B)** Quantification of the fluorescence intensity of Cav1-AH, Arfgap1-AH, and Plin1_108-137-AH at the surface of SQ and TO droplets, normalized by the fluorescence intensity on TO droplets for each AH. *t* test shows a significant difference between SQ and TO data ($P < 0.001$). Data are represented as mean ± SD. **(C)** Left: Quantification of the fluorescence intensity of Cav1-AH (green) and Plin1_108-137-AH (gray) at the surface of SE-TO (SE/TO, 1–3, wt/wt) and TO droplets, normalized by the fluorescence intensity on TO droplets. *t* test shows no significant difference between SE/TO (1/3) and TO data for both Cav1-AH and Plin1_108-137-AH ($P > 0.1$). Corresponding micrographs are shown in Fig. S5 B. Middle: Quantification of fluorescence intensity of Cav1-AH and Plin1_108-137-AH at the surface of TO and diolein-TO mixtures (DO/TO, 1/9, 1/1, vol/vol), normalized by the fluorescence intensity of TO droplets. *t* test shows a significant difference between DO/TO (1/1) and TO data for Cav1-AH ($P < 0.0001$) but shows no significant difference between DO/TO (1/1) and TO data for Plin1_108-137-AH ($P = 0.07$). Corresponding micrographs are shown in Fig. S5 C. Right: Quantification of fluorescence intensity of Cav1-AH and Plin1_108-137-AH at the surface of TO and RP/TO (1/1, 1/0), normalized by the fluorescence intensity of TO droplets. *t* test shows significant differences between RP and TO, and RP/TO (1/1) and TO, for both Cav1-AH and Plin1_108-137-AH ($P < 0.0001$). Corresponding micrographs are shown in Fig. S5 E. **(D)** Quantification of the fluorescence intensity of Cav1-AH (dark green), Cav1-AH(F2L,F8L) (green), and Cav1-AH(V5R) (light green) at the surface of SQ and TO droplets, normalized by the fluorescence intensity on TO droplets. Corresponding micrographs are shown in Fig. S5 G. *t* test shows significant differences between SQ and TO data for Cav1-AH, Cav1-AH(F2L,F8L), and Cav1-AH(V5R) ($P < 0.0001$). F-test of variance shows significant differences between SQ and TO data for both Cav1-AH and Cav1-AH(F2L,F8L) ($P = 0.0052$ and $P < 0.0001$, respectively) but no significative difference between SQ and TO for Cav1-AH(V5R) ($P = 0.8824$).

increased when the oil/buffer surface tension was higher (Fig. S5 I). However, within a given range of surface tensions, binding did not correlate with tension (Fig. S5 I). For Plin1_108-137, there was no correlation between the binding level and surface tension (Fig. S5 J). Altogether, these data suggest that the binding extent of an AH to a neutral lipid/buffer interface is driven by at least two contributions: a rough contribution of the ability of the AH to reduce the surface tension of the interface, and a fine-tuned contribution of the intrinsic interaction between the AH and the neutral lipid phase.

PLs control the accessibility of neutral lipids to AHs

During LD formation, the LD neutral lipid core is covered by a PL monolayer mainly deriving from the ER cytoplasmic leaflet. After emerging from the ER, LDs can grow or shrink, meaning that their PL monolayer density may vary, especially if they are physically disconnected from the ER membrane (Wilfling et al., 2014). Variation of the PL monolayer density will affect the accessibility of AHs to the oil-buffer interface. We hence wanted to understand the contribution of the PL packing density on AH binding level.

To characterize how the PL monolayer density modulates binding, we made neutral lipid-in-buffer aLDs with heterogenous coverage in PC, to which 1% of Cy5-PE was added. Cy5 signal was hence a reporter for the PL density at each aLD surface (Fig. 4 A). We next added Cav1-AH into the solution and recorded its recruitment over time (Fig. 4 A). Recruitment to aLDs presenting a lower PL density was more pronounced in both TO and SQ (Fig. 4 A, right; and Fig. S6, A and B, right). However, for a given PL density, the plateau of maximum recruitment was higher for TO than for SQ (Fig. 4, B and C), consistent with our previous observations. This maximum recruitment was then reported for each PL density (Fig. 4 D). We found that increasing the PL density diminished binding to aLDs (Fig. 4 D, right) until a critical density above which the binding level became almost constant (Fig. 4 D, right, higher PL densities). We actually found that the relative recruitment level of the AH to SQ and TO droplets remained independent of the PL level (Fig. 4, D and E): at any PL density, the ratio of CAV1-AH signal between TO and SQ was almost constant, ~2.62 (Fig. S3 H). This result suggests that the PL packing density simply modulates the amount of accessible neutral lipids and does not have a

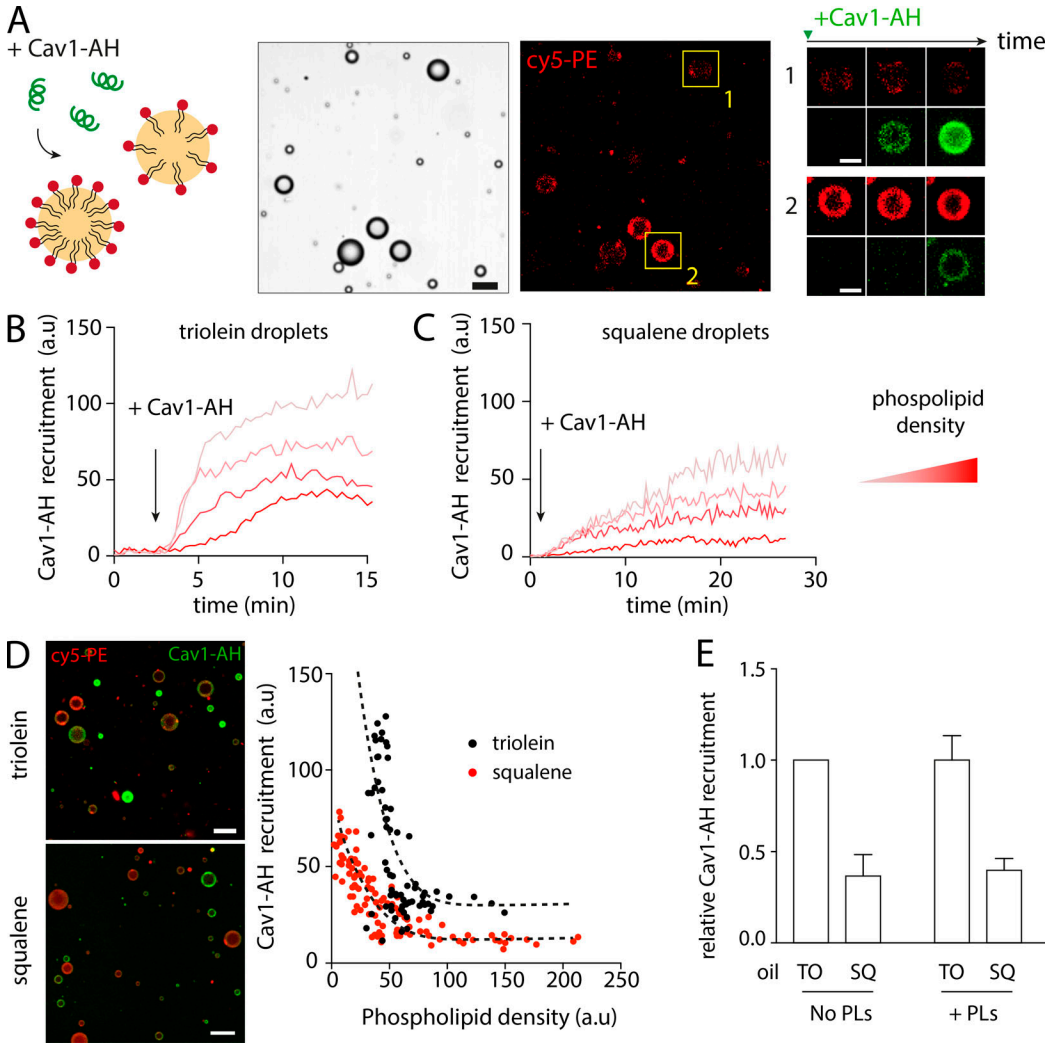

Figure 4. **PLs control the accessibility of neutral lipids to AHs. (A)** TO aLD with heterogeneous PL densities (DOPC:Cy5-DOPE; 99:1) were prepared in a buffer solution (see Cy5-DOPE channel, middle panel). NBD-tagged Cav1-AH was added to the bulk solution and the recruitment observed over time on aLDs presenting low (1) and high (2) PL density (right: time lapses of the droplets in yellow insets). Scale bars, 20 µm, and 10 µm for insets. **(B)** Cav1-AH recruitment over time to various TO droplets presenting different PL densities. Arrow indicates injection time of Cav1-AH to the bulk solution. The PL density evolves with red color darkness. Illustrative micrographs are shown in Fig. S6 A. **(C)** Cav1-AH recruitment over time on various SQ droplets presenting different PL densities. Arrow indicates injection time of Cav1-AH to the bulk solution. PL density varies with red color darkness. See Fig. S6 B for illustrative micrographs. Laser and microscope settings were identical for both SQ and TO experimental conditions. **(D)** Left: TO and SQ oil droplets supplemented with DOPC:Cy5-DOPE (99:1) were formed in buffer containing NBD tagged Cav1-AH. Droplets were imaged by confocal microscope after 30-min incubation time. Scale bar, 30 µm. Right: For both SQ and TO, cav1-AH recruitment over PL density shows a decrease as the PL density increases. Dashed lines are homothetical curve tendencies (with a factor of ∼2.62), indicating a constant relative recruitment between TO and SQ, independent of PL packing level. **(E)** Quantification of Cav1-AH recruitment on aLDs, with or without PLs at their surface. SQ over TO recruitment of Cav1-AH remains constant, independently of the presence of PLs at the droplet surface. Recruitment is normalized by the recruitment on TO droplets. For +PLs condition, Cav1-AH recruitment was averaged for a PL density around150 a.u. in D.

meaningful input in binding per se. These results reveal that the nature of the hydrophobic phase beneath a lipid layer is a major driving force to the binding of AHs (Fig. 5 A).

Based on all our above results, we propose a qualitative and illustrative phase diagram for the recruitment level of AHs based on their affinity to the lipid interface and the PL packing density (Fig. 5 B). The lipid interface could be either that of the neutral lipids or of the PL tails forming the intermonolayer space of a bilayer. A key feature of this diagram is that reaching a given binding level can be obtained by "slight" modulations of the interaction of the AH with the hydrophobic core, e.g., by a single mutation as seen with Cav1-AH in Fig. 1 J. In contrast, larger modulations of the PL packing density would be necessary to reach the same binding level by an AH of lower affinity. A good illustration of the latter point is Plin1_108-137-AH, which did not bind to aLDs connected to the bilayer (Fig. 1 I) but bound to isolated aLDs with ultra-loose PL packing (Fig. S1 F and Fig. S5 B).

PL acyl chain and shape modulate the recruitment of AHs to model LDs

PLs can have different membrane packing propensities and interactions with AHs. Hence, the PL nature could alter the

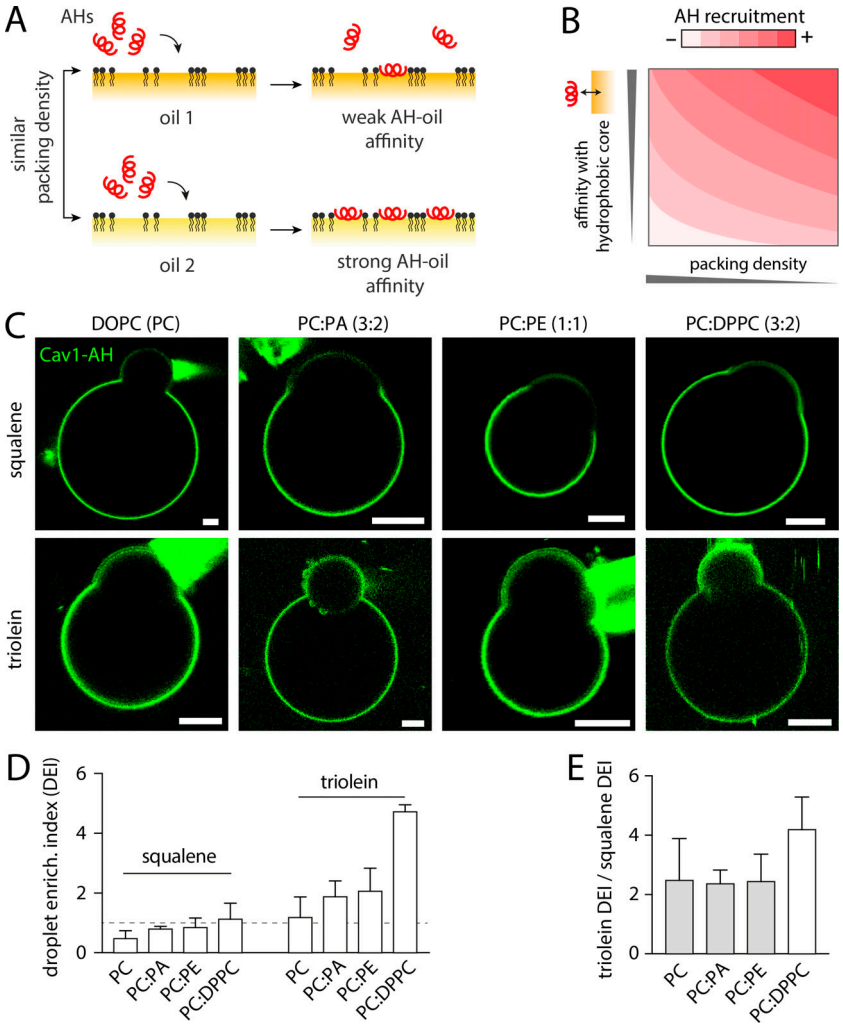

Figure 5. **PL acyl chain and shape regulates the preferential recruitment of AHs to aLDs. (A)** Illustration of the contribution of the neutral lipid type in AH recruitment. For a given PL packing level, an AH will be more recruited to the interface presenting the strongest AH-neutral lipid affinity. **(B)** Illustrative phase diagram showing the AH recruitment extent to the PL monolayer interface covering a hydrophobic region of a monolayer or a bilayer. This phase diagram takes into account the AH affinity for the hydrophobic region and PL packing density. **(C)** Representative confocal fluorescence images of DEVs made of SQ or TO and different PL composition, DOPC, DOPC-DOPA (3:2), DOPC-DOPE (1:1), DOPC-DPPC (3:2), and incubated with NBD tagged Cav1-AH. Scale bars, 5 µm. **(D)** Quantification of the droplet enrichment index for each condition shows a higher recruitment to TO than to SQ aLDs. Changing the PL composition of the DEV improves the recruitment, in PE, PA, and DPPC. **(E)** Ratio between the droplet enrichment index between TO and SQ droplets for a given DEV PL composition. The ratio is constant at ~2 between DOPC, DOPC-DOPA, and DOPC-DOPE, which have the same acyl tails. With DPPC, which has saturate acyl chains, the ratio is doubled.

binding level of AHs to LDs. We made DEVs containing dioleoyl DOPC (1,2-dioleoyl-sn-glycero-3-phosphocholine), DOPC/DOPE (1:1), or DOPC/DOPA (3:2). DOPE and DOPA had the same dioleoyl acyl chain as DOPC. We added Cav1-AH (Fig. 5 C) and determined the droplet enrichment index for TO and SQ conditions (Fig. 5 D). As compared with DOPC, the presence of DOPE and DOPA improved the enrichment index on the aLD for both neutral lipids. This improvement can be ascribed to the ability of DOPE and DOPA to generate more PL packing defects, due to their negative spontaneous curvature (Bigay and Antonny, 2012; Thiam et al., 2013b). The induced defects were probably identical on the bilayer and the aLD surface, because the relative binding to TO and SQ was constant, around 2, independent of DOPC, DOPE, and DOPA (Fig. 5 E).

The droplet enrichment index quantifies the recruitment to the aLD relative to the bilayer membrane of the DEV. If the bilayer recruitment is decreased, this index can be enhanced, while the net binding to the aLD may not be increased. In DOPC, DOPA, and DOPE, which have the same dioleoyl acyl chain, the interaction of the AH with the hydrophobic region of the bilayer, i.e., the PL acyl chains, is conserved between these PLs. We thus changed the PL acyl chain composition by making DEV with a mixture of DOPC, which has one unsaturation on each acyl chain, and DPPC (1,2-dipalmitoyl-sn-glycero-3-phosphocholine), which is fully saturated, at a ratio of 3:2. Cav1-AH was then added to the medium (Fig. 5 C), and we observed that the droplet enrichment index was drastically increased as compared with DOPC DEVs (Fig. 5 D). In TO, binding was increased by more than four times than in DOPC alone, while for SQ it was only doubled. The ratio of the droplet enrichment factor between TO over SQ was consequently increased (Fig. 5 E). This higher enrichment to the aLD in DPPC was likely due to a diminished recruitment of the peptide to the bilayer.

Altogether, our above results illustrate how alteration of membrane PL composition can shift the relative AH recruitment to the droplet surface to a greater extent. This can partly explain how AHs may be more recruited to LDs instead of bilayers. However, in the above experiments, a PL mixture was used, and we cannot exclude the possibility of a PL sorting between the bilayer and the aLD, which would make interpretation of the data difficult.

Discussion

The binding of AHs to membranes is regulated by several factors including membrane charges, packing defects, curvature, etc.

(Bigay and Antonny, 2012). On LDs, the PL packing density is so far the only lipid parameter found to regulate the binding of AHs (Bacle et al., 2017; Prévost et al., 2018; Thiam et al., 2013a), which depends also on the nature of the amphipathic sequence (Čopič et al., 2018; Prévost et al., 2018). Despite this understanding, it is still unclear how AHs specifically bind to LDs or LD subsets.

Here, we bring experimental evidence supporting that the LD surface is always less dense in PLs than a bilayer. Compared with 100 PLs on average on a monolayer of a bilayer, an aLD monolayer can bear up to a maximum of ∼87 PLs. This maximum is reached when the aLD is connected to the bilayer, which behaves as a PL reservoir. Therefore, LDs are more preset to recruit AHs than bilayers. However, our data show that this is not the whole picture since the nature of the hydrophobic phase, to which an AH has to bind, plays a crucial role in the recruitment. This hydrophobic phase would be PL acyl chains for a bilayer and neutral lipids for LDs. Thus, in addition to the higher PL packing defects on LDs, a more favorable interaction of an AH with the interface of neutral lipids than with PL acyl chains will promote more AH recruitment to LDs.

AHs may preferentially bind to LD subsets containing specific neutral lipids (Hsieh et al., 2012; Straub et al., 2008), and could therefore favor specific oil compositions. This is would be consistent with our data indicating that AHs may have differential affinities with neutral lipids, or at least to their interface with water (Fig. 3). For instance, the N-terminal AH of the lecithin retinol acyl transferase binds more tightly to retinol palmitate than to TO/water surface (Molenaar et al., 2019). On the contrary, Cav1-AH bound better to TO than to retinol palmitate or SQ/water interfaces. Diacylglycerols decreased Cav1-AH recruitment to TO interface but not for Plin1_108-137 (Fig. 3 C). These results support that the amphipathic sequence is crucial to the interactions with neutral lipids, beyond decreasing interfacial tension. This is particularly well illustrated by the ability of Cav1-AH and its F2L,F8L mutant to distinguish well between TO and SQ interfaces, but not the V5R mutant (Fig. 3 D). The question is therefore how amino acids can discern hydrophobic regions. Bulky hydrophobic residues typically facilitate the binding to both bilayers and LDs (Prévost et al., 2018; Wimley and White, 1993), because of the energy cost of exposing these residues to water. Hence, increasing the number of hydrophobic residues would basically decrease tension and hence annihilate specificity, as seen, for example, for NS5A (Fig. 1 I), or for Plin4 or CTP:phosphocholine cytidylyltransferase α mutations (Čopič et al., 2018; Prévost et al., 2018). Instead, to reach binding specificity, there might be amphipathic sequences that are well-tuned in hydrophobicity to decrease the neutral lipid/water surface tension enough without binding to bilayers and designed with an optimal interaction with a given neutral lipid. This seems to be at least the case for the most abundant LD proteins, Perilipin 1–5, whose 11-mer repeat AH sequence lacks bulky hydrophobic residues but can specifically detect LD surface (Ajjaji et al., 2019; Brasaemle, 2007; Čopič et al., 2018; Rowe et al., 2016). For instance, Perilipin 3 seems to better bind to LDs in the presence of diacylglycerols (Skinner et al., 2009).

Finally, the neutral lipid/water surface is permissive to the binding of any AH-containing protein, because of the high energy cost of exposing oil molecules to water, which is decreased by the adsorption of any amphiphilic molecules. Although all AHs may associate with bare neutral lipid/water interfaces, increasing the PL packing density will at some point specifically prevent the binding of AHs of weaker affinity, while those of higher affinity will still bind. For example, Cav1-AH and Plin1_108-137 both bound to the bare TO/buffer interface (Fig. 3 B), but only Cav1-AH bound to aLDs connected to the bilayer (Fig. 1 I). In cells, additional regulatory means can control the recruitment of AHs (Kory et al., 2016; Thiam and Dugail, 2019). For example, crowding of the LD surface by strongly bound proteins, such as Perilipin 1, or hairpin-containing proteins, enables prevention of the nonspecific adsorption of soluble AH-containing proteins (Ajjaji et al., 2019; Kory et al., 2015). Interactions with PL headgroups may also facilitate AH recruitment specificity. A good illustration of such regulation is provided by α-synuclein-AH, a lipid packing sensor that also localizes to LDs (Outeiro and Lindquist, 2003). This AH has a poorly developed hydrophobic face that needs the presence of charged PLs to reveal its ability to target to membrane packing defects (Pranke et al., 2011). AH–AH interactions, or AH interactions with other LD proteins, may also improve the binding selectivity (Kory et al., 2016; Thiam and Dugail, 2019).

In conclusion, our data highlight an undervalued contribution of neutral lipids in controlling the binding of AHs to the surface of LDs. The PL packing density simply regulates the amount of exposed neutral lipids. which dictates the binding level of AHs. Clearly, the full picture of how AHs selectively bind to LDs in a cellular context remains not completely resolved yet, but our data bring us a major step closer to it.

Materials and methods

DEV preparation: giant unilamellar vesicles (GUVs) + LDs

Unless mentioned otherwise, experiments were performed in the following HKM buffer: 50 mM Hepes, 120 mM K acetate, and 1 mM $MgCl_2$ (in Milli-Q water) at pH 7.4 and 275 ± 15 mOsm.

GUVs were prepared by electro-formation (Thiam et al., 2013a). PLs and mixtures thereof in chloroform at 0.5 µM were dried on an indium tin oxide–coated glass plate. The lipid film was desiccated for 1 h. The chamber was sealed with another indium tin oxide–coated glass plate. The lipids were then rehydrated with a sucrose solution (275 ± 15 mOsm). Electroformation is performed using 100 Hz AC voltage at 1.0 to 1.4 Vpp and maintained for at least 1 h. This low voltage was used to avoid hydrolysis of water and dissolution of the titanium ions on the glass plate. GUVs were either stored in the chamber at 4°C overnight or directly collected with a Pasteur pipette.

GUVs composition for used PLs mixtures were as follows: DOPC GUVs were 100% DOPC. Nickel DOPC GUVs were 99% DOPC, 1% DGS NTA(Ni). DOPE-DOPC GUVs were 50% DOPE, 50% DOPC. DOPA-DOPC GUVs were 40% DOPA, 60% DOPC. DPPC-DOPC GUVs were 40% DPPC, 60% DOPC.

To prepare the aLDs, 5 µl of the oil (TO, SQ, or dodecane) was added to 45 µl of HKM buffer. The mixture was sonicated. The diameter of the resulting droplets is on the order of a few hundred nanometers. To make DEV, GUVs were then incubated

with the LDs for 5 min. The GUV-LD mixture was then placed on a glass coverslip pretreated with 10% (wt/wt) BSA and washed three times with buffer.

Confocal microscope images

All micrographs of DEV were made on a Carl Zeiss LSM 800 with a 63× oil immersion objective, and observed samples were held by glass coverslips (Menzel Glaser; 24 × 36 mm, no. 0). Micrographs of oil droplets were made on a Carl Zeiss LSM 800 with a 10× air objective.

Micromanipulation and surface tension measurements by microaspiration

Micropipettes were made from capillaries drawn out with a Sutter Instruments pipette puller. They were used to manipulate the LD-embedded GUVs in order to get a side view of the system. The pipettes were incubated for 30 min in a 5% BSA solution before use, in order to prevent droplets and membranes from adhering to the glass.

Additionally, surface tensions were measured using the same pipettes (Fig. 1 B). The micromanipulation of the external LD monolayer enables the measurement of the external monolayer surface tension. Using Laplace's law, and the measurement of the pipette inner diameter, droplet diameter, and suction pressure, the surface tension of the interface can be determined:

$$\gamma = \frac{\Delta Psuc}{2\left(\frac{1}{Rp} - \frac{1}{Rd}\right)},$$

where $\Delta Psuc$, Rp, and Rd are the suction pressure, the pipette radius, and the droplet external radius, respectively.

The suction was performed using a syringe. The resulting pressure was measured with a pressure transducer, the output voltage of which was monitored with a digital voltmeter. The pressure transducer (range, 55 kPa) was calibrated before the experiments. Micropipettes were made from capillaries (1.0 OD × 0.58 ID × 150 L mm 30–0017 GC100-15b; Harvard Apparatus) with a micropipette puller (Sutter Instrument model P-2000). The micromanipulators used were TransferMan 4r, purchased from Eppendorf. The pressure transducer used was DP103, provided by Validyne Engineering Corp.

Peptide and protein recruitment on the DEV and oil droplets

The DEVs were held by a glass micropipette and observed by confocal microscopy. 5 µl of peptide or protein solution was injected in the 100 µl bulk phase of the DEV solution. The resulting effective peptide concentrations were, respectively, Arf1 (1 µM); caveolin-AH aa159–178 (5 µM); Arfgap1-AH (3.6 µM); and Plin1 AH aa108–137 (50 µM). The DEV is then followed for ∼10 min. Solutions were injected at similar spots from a pipette. Note that for Arfgap1-AH, due to peptide solubility issues, the buffer pH was lowered to 5.5.

Tagging PL with histidine mCherry fluorescent protein

Nickel DOPC GUVs were produced by electro-formation with a mixture of 99% DOPC and 1% DGS-Ni-NTA (wt/wt). DEVs were made using these GUVs. 5 µl of a histidine mCherry at 2.2 µM stock solution was added to 100 µl of the DEV solution and homogenated for 5 min. The resulting solution was placed on a coverslip (pretreated with 10% [wt/wt] BSA and washed three times with buffer). After 5 min, the red fluorescent histidine polluting the coverslip in the observation zone was laser bleached. DEV were brought with a micromanipulator into the clean observation zone and imaged at the apex, i.e., at the coverslip upper surface.

Pendent droplet interface characterization and surface tension measurements

A pendent droplet tensiometer designed by Teclis Instruments was used to measure the interfacial tension of oil/water interfaces. All experiments were conducted at room temperature. To create oil-buffer interfaces, oil drops (from 5 to 16.0 µl) were formed at the tip of a J-needle submerged in 5 ml of HKM buffer.

Oil-buffer interface tension measurement

After forming an oil droplet, the surface tension of the interface is measured until it stabilizes to a plateau. This plateau of tension is the tension designated as the bare oil-buffer surface tension.

Oil-PL interface characterization

To create PL monolayers at the oil-water interface, 100 µl of DOPC liposomes solution were added to the 5-ml HKM buffer. After forming a droplet, the PLs relocate at the interface. Sinusoidal area oscillations are applied to the droplet for 10 cycles as the interfacial tension is recorded. This allows us to calculate the elastic modulus of the interface E (mN/m). Then the droplet is compressed in order to increase the lateral pressure (π) in the PL monolayer, and sinusoidal area oscillations are applied to the droplet for another 10 cycles. This method is reproduced for various lateral pressures, allowing us to build an elastic modulus (E) over lateral pressure (π) isotherm. This isotherm is then fitted using the theoretical Frumkin isotherm and enables us to get an estimation of the molecular area of PLs at the interface.

Frumkin isotherm model and molecular area extraction

The Frumkin isotherm model leads to the following expression of the elastic modulus of a PL monolayer (E) related to the lateral pressure of this same monolayer (π; Kolev et al., 2002):

$$\pi = -RT\,\Gamma_\infty\left[Ln\left(1-\frac{\Gamma}{\Gamma_\infty}\right) - \frac{h\,\Gamma^2}{RT\,\Gamma_\infty{}^2}\right],$$

$$E = RT\,\Gamma_\infty\left[1-\frac{\Gamma}{\Gamma_\infty\left(1-\frac{\Gamma}{\Gamma_\infty}\right)} + 2\frac{h\,\Gamma^2}{RT\,\Gamma_\infty{}^2}\right].$$

The parameters appearing in these two expressions are Γ, the molar PL surface density of the interface; Γ_∞, molar PL surface density extrapolated at the infinite compression; R, the perfect gas constant; T, the temperature; and h, the absorption enthalpy of PL at the oil buffer interface.

By modulating h and Γ_∞ to fit the experimental E-π curve obtained following the protocol described in Pendent droplet interface characterization..., it is then possible to get access to an estimation of the PL density at the interface Γ and to easily obtain the evolution of the molecular area of the PLs.

Oil in water PL-free droplet

To simultaneously observe a micrometric-size droplet constituted of different oil under the confocal microscope, we used two micropipettes, prefilled with two different oil types, and connected to syringes. The pipettes were introduced in a buffer medium placed under a confocal microscope. By pressing on the syringes, multiple droplets of two different compositions were formed in the observation field. The peptide was then added to the medium and peptide recruitment observed by fluorescence.

Oil in water droplet covered with PLs

DOPC PLs in chloroform were dried under argon and oil was added in such proportion to obtain a molar ratio of 0.1%. The mix was then sonicated for 10 min and 100 µl of HKM buffer was then added to 10 µl of oil and gently agitated to obtain the micron-size droplets observed under microscope.

GUV under osmotic shock

DOPC GUVs were produced by electro-formation with a mixture of 99% DOPC and 1% (wt/wt) rhodamine-DOPE (wt/wt). The resulting GUV solution was placed on a coverslip (pretreated with 10% [wt/wt] BSA and washed three times with buffer) and observed with a confocal microscope (10× objective). 20 µl Ultrapure Milli-Q water was added for 100 µl of the GUV solution. GUVs were then imaged over time. GUV radius was measured over time.

Surface tension of different oil-water interface

Surface tension of oil buffer interface was measured using pendent droplet tensiometer except for silicone oil (tension from Mazurek, 2007), PFOB (Astafyeva et al., 2015 and our measurement using pendent droplet tensiometer), and diolein-TO mix (Shimada and Ohashi, 2003).

Quantification and statistical analysis

Fluorescent signal quantification at GUV or aLD surface

To quantify the recruitment of the fluorescent peptides at the surface of LDs, we used the radial angle profile plugin of ImageJ software. This plugin measures the average signal intensity along the perimeter of concentric circles. It results in a plot of the intensity profile of a circular object for various positions relative to its center. We chose the maximum intensity profile as a measurement of recruited peptide density. The same method was used to quantify the PL density covering oil droplet.

Determination of the optical corrective parameter (β), related to Fig. S2

Due to experimental limitations, the DEVs used in this study were mainly imaged along their equatorial cross-section, an easier configuration when using micropipettes for manipulation. However, when measuring the fluorescence signal of aLDs at this equatorial level, we found a significant attenuation as compared with the signal measured at the apex of the droplet (Fig. S2 A). This is very likely due to the mismatch in optical index between the bulk water phase and the oil phase of the droplet (with 63× objective).

To investigate this attenuation effect, we imaged a single oil droplet homogeneously marked with histidine mCherry (Fig. S2 D). We noticed that the intensity of confocal fluorescence signal was varying along the z axis (Fig. S2 D, left). We quantified this signal modification with intensity-linescans at different z positions (see Fig. S2 D, right). The signal was maximum at the lower apex plane, i.e., bottom of the droplet, and almost dimmed just above the equatorial position (see third slice, Fig. S2 D). We reasonably assumed that this effect was due to the refraction of the laser light by the refractive index variation at the droplet–buffer interface. Indeed, when imaged at the lower apex, the light beam from the microscope objective is directly reflected back to the imaging system. On the contrary, when the droplet is imaged at or above the equatorial cross-section, part of the light has to pass through the oil phase of the droplet and is certainly disrupted by the optical index mismatch, leading to the observed signal attenuation (Fig. S2, A and D).

Therefore, the signal measured at the apex (not affected by the optical index mismatch) is to be considered as the correct measurement of the fluorescent signal on the droplet. On the contrary, to get the real signal on the droplet at the equatorial cross-section, the measured signal has to be corrected.

To quantify the signal attenuation at the equatorial cross-section, we imaged various DEV at the equatorial cross-section and the apex. We normalized the droplet signal by the bilayer signal (Fig. S2 B) and compared the normalized signal measured at the apex and the equatorial cross-section. We found an average of 2.67 times less signal at the equatorial cross-section as compared with the apex.

We thus defined a correcting optical parameter β as the apex normalized signal divided by the equatorial cross-section normalized signal (Fig. S2 C), which was therefore equal to 2.67. To properly evaluate the fluorescence on aLDs imaged at the equatorial cross-section, the measured signal then had to be multiplied by the optical parameter $\beta = 2.67$.

As some of the DEVs used in this study were made with SQ oil droplets, we performed similar experiments on such systems and found comparable results (Fig. S2 E). The fluorescence signal attenuation between apex (focal plane 1) and equatorial cross-section (focal plane 2) was found at 2.7 (Fig. S2 E, right), a value comparable to those obtained with TO droplets in Fig. S2 B.

Statistical analysis

The statistical comparisons were made using a nonparametric *t* test (GraphPad Prism 7.0a; ***, $P < 0.0001$; **, $P < 0.001$; *, $P < 0.01$). Unless mentioned, all values shown in the text and figures are mean ± SD.

Equipment and reagents

Equipment

Imaging was done using a Carl Zeiss LSM 800 microscope and a 63× objective. Glass coverslips were obtained from Menzel Glaser (24 × 36 mm, no. 0). Micropipettes were made from capillaries (1.0 OD × 0.58 ID × 150 L mm 30–0017 GC100-15b), purchased from Harvard Apparatus; they were stretched by using a micropipette puller from Sutter Instrument (model P-2000). Micromanipulators TransferMan 4r were purchased from Eppendorf. The pressure transducer used was DP103, provided by Validyne Engineering Corp. The pendent droplet tensiometer apparatus was from Teclis Instruments.

Chemical product list

Glyceryl trioleate (TO; T7140), dodecane (297879-1L), SQ (S3626), SE (C9253 1G), monoolein (1-oleoyl-rac-glycerol M7765), retinylpalmitate (RP; R3375), Hepes (54457–250-F), K acetate (P1190), $MgCl_2$ (M8266-100G), BSA 98% (A7906-100G), and sucrose 99.5% (59378-500G) were from Sigma-Aldrich. Perfluorooctyl bromide (AB104047, CAS: 423–55-2) was purchased from Abcr GmbH. Silicone oil (polydimethylsiloxane, 20cSt, ref 84543–290) was purchased from VWR Chemical. Dioleine (800811C, 10 mg dioleyl-sn-glycerol 18–1) was from Avanti Polar Lipids.

PLs, DOPC, DOPE, DOPA, DPPC, DGS-Ni-NTA, rhodamine-DOPE, and cy5-DOPE were from Avanti Polar Lipids.

Peptide and protein origin or production methods

Caveolin fragment tag with NBD refered to as Cav1-AH (fragment 159–178, purity 96.83%, NBD-LFEAVGKIFSNVRINLQKEI), corresponding mutant Cav1-AH(F2L,F8L) (purity 99.28% NBD-ahx-LLEAVGKILSNVRINLQKEI) and Cav1-AH(V5R) (purity 95.33% NBD-ahx-LFEARGKIFSNVRINLQKEI), and Arfgap1 modified fragment tagged with rhodamine refered to as Arfgap1-AH (fragment 199–223, purity 95.49%, rhodamineB-FLNSAMSSLYSGWSSFTTRAKKFAK) were synthesized by Peptide 2.0 (https://www.peptide2.com/).

Plin1 108–137, purity 96.83% (NBD-PPEKIASELKDTISTRLRSARNSISVPIAS), was purchased from ProteoGenix (https://www.proteogenix.science/fr/).

NS5A peptide (rhodamine-SGSWLRDVWDWVCTILTDFKNWLTSKLFPKL-CONH), which is the N-terminal AH of the nonstructural protein 5 of the hepatitis C virus, was provided by F. Penin, University of Lyon, Lyon, France.

Fluorescently labeled Arf1 was generated using an Arf1 variant in which the single cysteine residue of Arf1 was replaced with serine, and the C-terminal lysine was replaced with cysteine, yielding Arf1-C159S-K181C. Published work has demonstrated that exchanging the C-terminal lysine of the small GTPase with a Cys residue, and subsequent fluorescent labeling (using thiol-reactive dyes on Cys181) does not inhibit Arf1 function (Beck et al., 2008). In short, human Arf1-C159S-K181C and yeast N-myristoyltransferase were coexpressed in *Escherichia coli* supplied with BSA-loaded myristate. Cell lysates were subjected to 35% ammonium sulfate, and the precipitate, enriched in myristoylated Arf1, was further purified by DEAE-ion exchange. Eluted fractions of interest were concentrated in spin-column filters with a 10-kD cutoff (Millipore), and fluorescently labeled using Cy3-maleimide (GE Healtcare) according to the manufacturer's protocol. To remove excess dye, samples were purified by gel filtration using a Superdex 75 column (GE Healthcare).

Online supplemental material

Fig. S1 displays micrographs and quantification of various AHs recruitment on TO, dodecane, and SQ DEVs, related to Fig. 1. Fig. S2 describes the experimental determination of the optical correction factor β accounting for the optical index mismatch between the oil droplet and the external water phase. The methodology for determining the optical correction factor β accounting for the optical index mismatch between the oil droplet and the external water phase is described in the Materials and methods section. The figure is related to Fig. 2. Fig. S3 displays complementary experiments for the determination of the PL density in DEV by using tagged PLs and the pending droplet experiment. Dodecane and TO-SE oil mixtures are investigated. The figure is related to Fig. 2. Fig. S4 presents the pendent droplet experimental raw data used for the determination of the area per PL as a function of the lateral pressure. The figure is related to Fig. 2. Fig. S5 displays confocal micrographs corresponding to the quantification of recruitment of AHs to bare oil droplets of various oil compositions. The recruitment as a function of tension is presented. The figure is related to Fig. 3. Fig. S6 shows the recruitment time-lapse of Cav1-AH to TO and SQ droplets of various PL densities. The figure is related to Fig. 4.

Acknowledgments

We are thankful to all the group members for their valuable comments and critical discussions. We also thank Dr. Alain Cagna for helpful discussion and Dr. Alenka Copic for the critical read of the manuscript.

This work was supported by grants from the Agence Nationale de la Recherche (ANR-17-CE11-0003-NANODROP and ANR-18-CE11-0012-01-MOBIL), and by the Paris Sciences et Lettres to A.R. Thiam.

The authors declare no competing financial interests.

Author contributions: A.R. Thiam designed research. A. Chorlay performed experiments. A.R. Thiam and A. Chorlay analyzed data and wrote the manuscript.

Submitted: 15 July 2019
Revised: 14 December 2019
Accepted: 27 January 2020

References

Ajjaji, D., K. Ben M'barek, M.L. Mimmack, C. England, H. Herscovitz, L. Dong, R.G. Kay, S. Patel, V. Saudek, D.M. Small, et al. 2019. Dual binding motifs underpin the hierarchical association of perilipins1-3 with lipid droplets. *Mol. Biol. Cell.* 30:703–716. https://doi.org/10.1091/mbc.E18-08-0534

Antonny, B., S. Beraud-Dufour, P. Chardin, and M. Chabre. 1997. N-terminal hydrophobic residues of the G-protein ADP-ribosylation factor-1 insert into membrane phospholipids upon GDP to GTP exchange. *Biochemistry.* 36:4675–4684. https://doi.org/10.1021/bi962252b

Astafyeva, K., W. Urbach, N. Garroum, N. Taulier, and A.R. Thiam. 2015. Stability of C(12)E(j) Bilayers Probed with Adhesive Droplets. *Langmuir.* 31:6791–6796. https://doi.org/10.1021/acs.langmuir.5b00749

Bacle, A., R. Gautier, C.L. Jackson, P.F.J. Fuchs, and S. Vanni. 2017. Interdigitation between triglycerides and lipids modulates surface properties of lipid droplets. *Biophys. J.* 112:1417–1430. https://doi.org/10.1016/j.bpj.2017.02.032

Beck, R., Z. Sun, F. Adolf, C. Rutz, J. Bassler, K. Wild, I. Sinning, E. Hurt, B. Brügger, J. Béthune, and F. Wieland. 2008. Membrane curvature induced by Arf1-GTP is essential for vesicle formation. *Proc. Natl. Acad. Sci. USA.* 105:11731–11736. https://doi.org/10.1073/pnas.0805182105

Ben M'barek, K., D. Ajjaji, A. Chorlay, S. Vanni, L. Forêt, and A.R. Thiam. 2017. ER Membrane Phospholipids and Surface Tension Control Cellular Lipid Droplet Formation. *Dev. Cell.* 41:591–604.e7. https://doi.org/10.1016/j.devcel.2017.05.012

Bersuker, K., and J.A. Olzmann. 2017. Establishing the lipid droplet proteome: Mechanisms of lipid droplet protein targeting and degradation. *Biochim Biophys Acta Mol Cell Biol Lipids*. 1862(10 Pt B):1166–1177. https://doi.org/10.1016/j.bbalip.2017.06.006

Bigay, J., and B. Antonny. 2012. Curvature, lipid packing, and electrostatics of membrane organelles: defining cellular territories in determining specificity. *Dev. Cell*. 23:886–895. https://doi.org/10.1016/j.devcel.2012.10.009

Bigay, J., J.-F. Casella, G. Drin, B. Mesmin, and B. Antonny. 2005. ArfGAP1 responds to membrane curvature through the folding of a lipid packing sensor motif. *EMBO J.* 24:2244–2253. https://doi.org/10.1038/sj.emboj.7600714

Blaner, W.S., S.M. O'Byrne, N. Wongsiriroj, J. Kluwe, D.M. D'Ambrosio, H. Jiang, R.F. Schwabe, E.M. Hillman, R. Piantedosi, and J. Libien. 2009. Hepatic stellate cell lipid droplets: a specialized lipid droplet for retinoid storage. *Biochim. Biophys. Acta*. 1791:467–473. https://doi.org/10.1016/j.bbalip.2008.11.001

Brasaemle, D.L. 2007. Thematic review series: adipocyte biology. The perilipin family of structural lipid droplet proteins: stabilization of lipid droplets and control of lipolysis. *J. Lipid Res.* 48:2547–2559. https://doi.org/10.1194/jlr.R700014-JLR200

Chorlay, A., and A.R. Thiam. 2018. An asymmetry in monolayer tension regulates lipid droplet budding direction. *Biophysical journal*. 114(3): 631–640. https://doi.org/10.1016/j.bpj.2017.12.014

Chorlay, A., L. Monticelli, J. Veríssimo Ferreira, K. Ben M'barek, D. Ajjaji, S. Wang, E. Johnson, R. Beck, M. Omrane, M. Beller, et al. 2019. Membrane asymmetry imposes directionality on lipid droplet emergence from the ER. *Dev. Cell*. 50:25–42.e7. https://doi.org/10.1016/j.devcel.2019.05.003

Čopič, A., S. Antoine-Bally, M. Giménez-Andrés, C. La Torre Garay, B. Antonny, M.M. Manni, S. Pagnotta, J. Guihot, and C.L. Jackson. 2018. A giant amphipathic helix from a perilipin that is adapted for coating lipid droplets. *Nat. Commun.* 9:1332. https://doi.org/10.1038/s41467-018-03717-8

Fainerman, V.B., R. Miller, and V.I. Kovalchuk. 2002. Influence of the Compressibility of Adsorbed Layers on the Surface Dilational Elasticity. *Langmuir*. 18:7748–7752. https://doi.org/10.1021/la020024e

Gannon, J., J. Fernandez-Rodriguez, H. Alamri, S.B. Feng, F. Kalantari, S. Negi, A.H. Wong, A. Mazur, L. Asp, A. Fazel, et al. 2014. ARFGAP1 is dynamically associated with lipid droplets in hepatocytes. *PLoS One*. 9: e111309. https://doi.org/10.1371/journal.pone.0111309

Guo, Y., T.C. Walther, M. Rao, N. Stuurman, G. Goshima, K. Terayama, J.S. Wong, R.D. Vale, P. Walter, and R.V. Farese. 2008. Functional genomic screen reveals genes involved in lipid-droplet formation and utilization. *Nature*. 453:657–661. https://doi.org/10.1038/nature06928

Henne, W.M., M.L. Reese, and J.M. Goodman. 2018. The assembly of lipid droplets and their roles in challenged cells. *EMBO J.* 37:e98947. https://doi.org/10.15252/embj.201898947

Hsieh, K., Y.K. Lee, C. Londos, B.M. Raaka, K.T. Dalen, and A.R. Kimmel. 2012. Perilipin family members preferentially sequester to either triacylglycerol-specific or cholesteryl-ester-specific intracellular lipid storage droplets. *J. Cell Sci.* 125:4067–4076. https://doi.org/10.1242/jcs.104943

Kassan, A., A. Herms, A. Fernández-Vidal, M. Bosch, N.L. Schieber, B.J. Reddy, A. Fajardo, M. Gelabert-Baldrich, F. Tebar, C. Enrich, et al. 2013. Acyl-CoA synthetase 3 promotes lipid droplet biogenesis in ER microdomains. *J. Cell Biol.* 203:985–1001. https://doi.org/10.1083/jcb.201305142

Kolev, V.L., K.D. Danov, P.A. Kralchevsky, G. Broze, and A. Mehreteab. 2002. Comparison of the van der Waals and Frumkin adsorption isotherms for sodium dodecyl sulfate at various salt concentrations. *Langmuir*. 18: 9106–9109. https://doi.org/10.1021/la0259858

Kory, N., A.-R. Thiam, R.V. Farese Jr., and T.C. Walther. 2015. Protein crowding is a determinant of lipid droplet protein composition. *Dev. Cell*. 34:351–363. https://doi.org/10.1016/j.devcel.2015.06.007

Kory, N., R.V. Farese Jr., and T.C. Walther. 2016. Targeting fat: mechanisms of protein localization to lipid droplets. *Trends Cell Biol.* 26:535–546. https://doi.org/10.1016/j.tcb.2016.02.007

Kralchevsky, P.A., K.D. Danov, and N.D. Denkov. 2008. Chemical physics of colloid systems and interfaces. *In* Handbook of Surface and Colloid Chemistry. CRC Press, Boca Raton, FL. 204–384.

Kučerka, N., J.F. Nagle, J.N. Sachs, S.E. Feller, J. Pencer, A. Jackson, and J. Katsaras. 2008. Lipid bilayer structure determined by the simultaneous analysis of neutron and X-ray scattering data. *Biophys. J.* 95:2356–2367. https://doi.org/10.1529/biophysj.108.132662

Mazurek, M.H. 2007. Silicones. *In* Comprehensive Organometallic Chemistry III. D.M.P. Mingos, and R.H. Crabtree, editors. Elsevier Science, Amsterdam. 651–697. https://doi.org/10.1016/B0-08-045047-4/00052-2

Molenaar, M.R., T.A. Wassenaar, K.K. Yadav, A. Toulmay, M.C. Mari, L. Caillon, A. Chorlay, M.W. Haaker, R.W. Wubbolts, and M. Houweling. 2019. Lecithin: Retinol Acyl Transferase (LRAT) induces the formation of lipid droplets. *bioRxiv*. (preprint posted August 14, 2019). https://doi.org/10.1101/733931

Olzmann, J.A., and P. Carvalho. 2019. Dynamics and functions of lipid droplets. *Nat. Rev. Mol. Cell Biol.* 20:137–155. https://doi.org/10.1038/s41580-018-0085-z

Outeiro, T.F., and S. Lindquist. 2003. Yeast cells provide insight into alpha-synuclein biology and pathobiology. *Science*. 302:1772–1775. https://doi.org/10.1126/science.1090439

Pranke, I.M., V. Morello, J. Bigay, K. Gibson, J.-M. Verbavatz, B. Antonny, and C.L. Jackson. 2011. α-Synuclein and ALPS motifs are membrane curvature sensors whose contrasting chemistry mediates selective vesicle binding. *J. Cell Biol.* 194:89–103. https://doi.org/10.1083/jcb.201011118

Prévost, C., M.E. Sharp, N. Kory, Q. Lin, G.A. Voth, R.V. Farese Jr., and T.C. Walther. 2018. Mechanism and determinants of amphipathic helix-containing protein targeting to lipid droplets. *Dev. Cell*. 44:73–86.e4. https://doi.org/10.1016/j.devcel.2017.12.011

Reddy, A.S., D.T. Warshaviak, and M. Chachisvilis. 2012. Effect of membrane tension on the physical properties of DOPC lipid bilayer membrane. *Biochim. Biophys. Acta*. 1818:2271–2281. https://doi.org/10.1016/j.bbamem.2012.05.006

Rowe, E.R., M.L. Mimmack, A.D. Barbosa, A. Haider, I. Isaac, M.M. Ouberai, A.R. Thiam, S. Patel, V. Saudek, S. Siniossoglou, and D.B. Savage. 2016. Conserved amphipathic helices mediate lipid droplet targeting of perilipins 1–3. *J. Biol. Chem.* 291:6664–6678. https://doi.org/10.1074/jbc.M115.691048

Senkal, C.E., M.F. Salama, A.J. Snider, J.J. Allopenna, N.A. Rana, A. Koller, Y.A. Hannun, and L.M. Obeid. 2017. Ceramide is metabolized to acylceramide and stored in lipid droplets. *Cell Metab.* 25:686–697. https://doi.org/10.1016/j.cmet.2017.02.010

Shi, S.T., S.J. Polyak, H. Tu, D.R. Taylor, D.R. Gretch, and M.M. Lai. 2002. Hepatitis C virus NS5A colocalizes with the core protein on lipid droplets and interacts with apolipoproteins. *Virology*. 292:198–210. https://doi.org/10.1006/viro.2001.1225

Shimada, A., and K. Ohashi. 2003. Interfacial and emulsifying properties of diacylglycerol. *Food Sci. Technol. Res.* 9:142–147. https://doi.org/10.3136/fstr.9.142

Shyu, P. Jr., X.F.A. Wong, K. Crasta, and G. Thibault. 2018. Dropping in on lipid droplets: insights into cellular stress and cancer. *Biosci. Rep.* 38: BSR20180764. https://doi.org/10.1042/BSR20180764

Skinner, J.R., T.M. Shew, D.M. Schwartz, A. Tzekov, C.M. Lepus, N.A. Abumrad, and N.E. Wolins. 2009. Diacylglycerol enrichment of endoplasmic reticulum or lipid droplets recruits perilipin 3/TIP47 during lipid storage and mobilization. *J. Biol. Chem.* 284:30941–30948. https://doi.org/10.1074/jbc.M109.013995

Spanova, M., and G. Daum. 2011. Squalene–biochemistry, molecular biology, process biotechnology, and applications. *Eur. J. Lipid Sci. Technol.* 113: 1299–1320. https://doi.org/10.1002/ejlt.201100203

Straub, B.K., P. Stoeffel, H. Heid, R. Zimbelmann, and P. Schirmacher. 2008. Differential pattern of lipid droplet-associated proteins and de novo perilipin expression in hepatocyte steatogenesis. *Hepatology*. 47: 1936–1946. https://doi.org/10.1002/hep.22268

Thiam, A.R., and M. Beller. 2017. The why, when and how of lipid droplet diversity. *J. Cell Sci.* 130:315–324. https://doi.org/10.1242/jcs.192021

Thiam, A.R., and I. Dugail. 2019. Lipid droplet-membrane contact sites - from protein binding to function. *J. Cell Sci.* 132:jcs230169. https://doi.org/10.1242/jcs.230169

Thiam, A.R., and L. Forêt. 2016. The physics of lipid droplet nucleation, growth and budding. *Biochim. Biophys. Acta*. 1861(8, 8 Pt A):715–722. https://doi.org/10.1016/j.bbalip.2016.04.018

Thiam, A.R., B. Antonny, J. Wang, J. Delacotte, F. Wilfling, T.C. Walther, R. Beck, J.E. Rothman, and F. Pincet. 2013a. COPI buds 60-nm lipid droplets from reconstituted water-phospholipid-triacylglyceride interfaces, suggesting a tension clamp function. *Proc. Natl. Acad. Sci. USA*. 110:13244–13249. https://doi.org/10.1073/pnas.1307685110

Thiam, A.R., R.V. Farese Jr., and T.C. Walther. 2013b. The biophysics and cell biology of lipid droplets. *Nat. Rev. Mol. Cell Biol.* 14:775–786. https://doi.org/10.1038/nrm3699

Vanni, S., H. Hirose, H. Barelli, B. Antonny, and R. Gautier. 2014. A sub-nanometre view of how membrane curvature and composition modulate lipid packing and protein recruitment. *Nat. Commun.* 5:4916. https://doi.org/10.1038/ncomms5916

Walther, T.C., and R.V. Farese Jr. 2012. Lipid droplets and cellular lipid metabolism. *Annu. Rev. Biochem.* 81:687–714. https://doi.org/10.1146/annurev-biochem-061009-102430

Walther, T.C., J. Chung, and R.V. Farese Jr. 2017. Lipid droplet biogenesis. *Annu. Rev. Cell Dev. Biol.* 33:491–510. https://doi.org/10.1146/annurev-cellbio-100616-060608

Welte, M.A. 2015. Expanding roles for lipid droplets. *Curr. Biol.* 25:R470–R481. https://doi.org/10.1016/j.cub.2015.04.004

Wilfling, F., A.R. Thiam, M.-J. Olarte, J. Wang, R. Beck, T.J. Gould, E.S. Allgeyer, F. Pincet, J. Bewersdorf, R.V. Farese Jr., and T.C. Walther. 2014. Arf1/COPI machinery acts directly on lipid droplets and enables their connection to the ER for protein targeting. *eLife.* 3:e01607. https://doi.org/10.7554/eLife.01607

Wimley, W.C., and S.H. White. 1993. Membrane partitioning: distinguishing bilayer effects from the hydrophobic effect. *Biochemistry.* 32:6307–6312. https://doi.org/10.1021/bi00076a001

Wolins, N.E., D.L. Brasaemle, and P.E. Bickel. 2006. A proposed model of fat packaging by exchangeable lipid droplet proteins. *FEBS Lett.* 580: 5484–5491. https://doi.org/10.1016/j.febslet.2006.08.040

JCB

Supplemental material

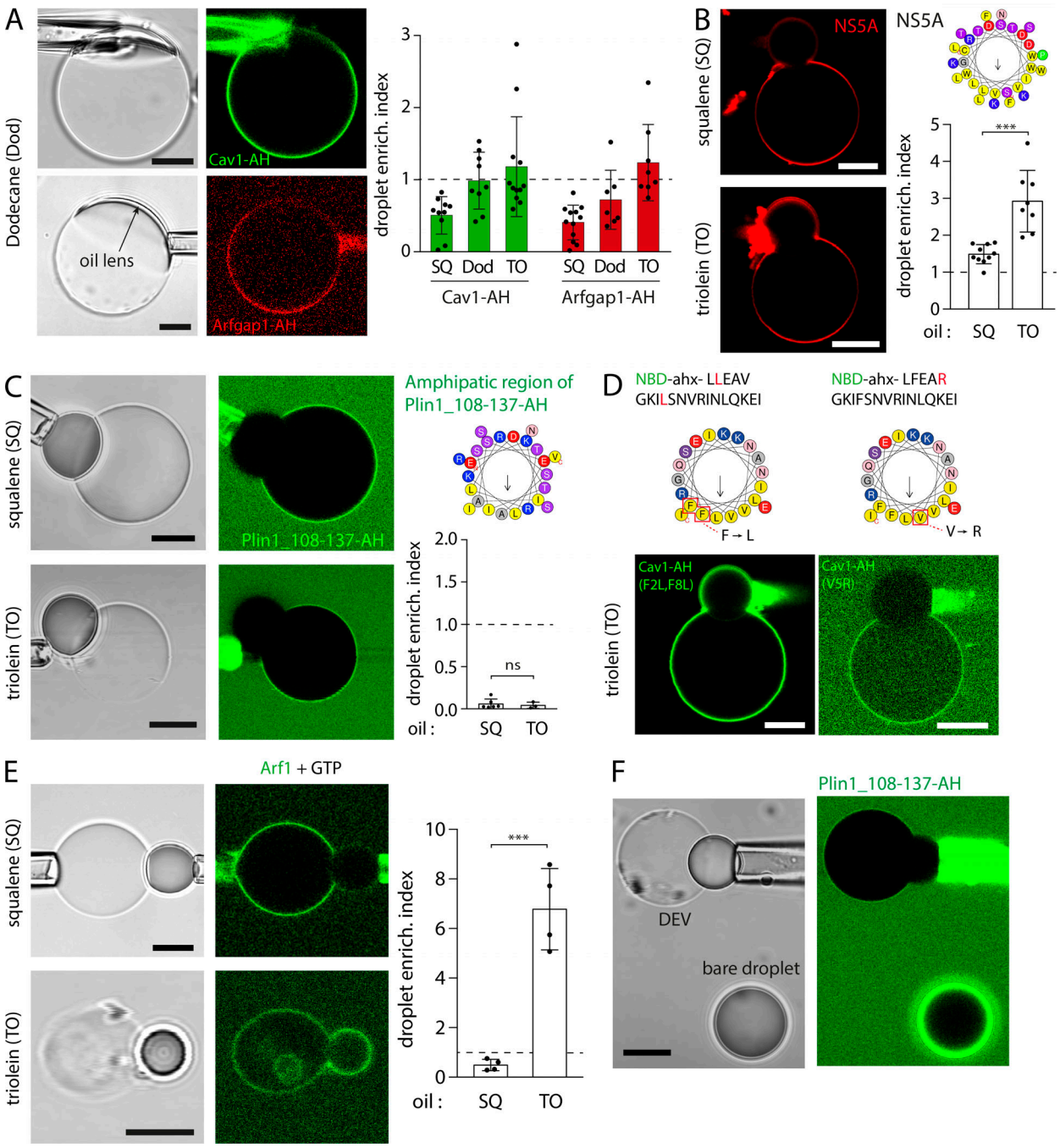

Figure S1. **Micrographs and quantification of various AHs recruitment on TO, dodecane, and SQ DEVs, related to Fig. 1. (A)** Left: DEV are produced using dodecane oil aLDs. Cav1-AH tagged with NBD and Arfgap1-AH tagged with rhodamine B recruitment to the dodecane interface is observed by confocal fluorescence microscopy. Scale bars, 10 µm. Right: Quantification of Cav1-AH and Arfgap1-AH droplet enrichment index for dodecane aLDs. SQ and TO droplet enrichment index are displayed for comparison. Data are represented as mean ± SD. Related to Fig. 1, E–H. **(B)** Left: A rhodamine-tagged NS5A-amphipatic helix (NS5A-AH) of the nonstructural protein 5 of the hepatitis C virus (see structure on the top right) is added to DEV solution. Micrographs show NS5A-AH recruited to DEVs containing SQ or TO aLDs. Scale bars, 10 µm. Bottom right: Quantification of droplet enrichment index for both SQ and TO aLDs. TO as compared with SQ recruited more Cav1-AH to the aLD. *t* test shows significant difference ($P < 0.001$). Data are represented as mean ± SD. **(C)** Left: Plin1 108–137 fragment (containing an AH region displayed on top right) tagged with NBD is added to a DEV solution. Micrographs show visible recruitment of Plin1(108–137)-AH to neither SQ nor TO aLDs. Scale bars, 10 µm. Bottom right: Quantification of Plin1(108–137)-AH droplet enrichment index for SQ an TO aLDs. Related to Fig. 1 I. **(D)** Top: Sequence and localization of mutated Cav1-AH: Cav1-AH(F2L,F8L) and Cav1-AH(V5R). Bottom: Cav1-AH(F2L,F8L) and Cav1-AH(V5R), tagged with NBD, are added to DEV solutions. Micrographs show recruitment of Cav1-AH(F2L,F8L) on TO aLDs but no recruitment of Cav1-AH(V5R). Scale bars, 10 µm. Related to quantification of Fig. 1 J. **(E)** Left: Arf1 full-length protein is added to a DEV solution containing GTP and EDTA. Micrographs show Arf1 recruited to the DEV surface containing SQ or TO aLDs. Scale bars, 10 µm. Right: Quantification of Arf1 droplet enrichment index for SQ and TO aLDs. TO aLDs recruited more Arf1 as compared with SQ droplets ($n = 1, 4$). **(F)** Plin1_108-137-AH, tagged with NBD, is added to a DEV solution (PC bilayer and TO-SE 3:1), which also contained bare TO-SE droplets, not covered by PC. Micrographs show no recruitment of Plin1(108–137)-AH on the aLD present in the DEV bilayer but strong recruitment to the bare droplet. Scale bar, 10 µm.

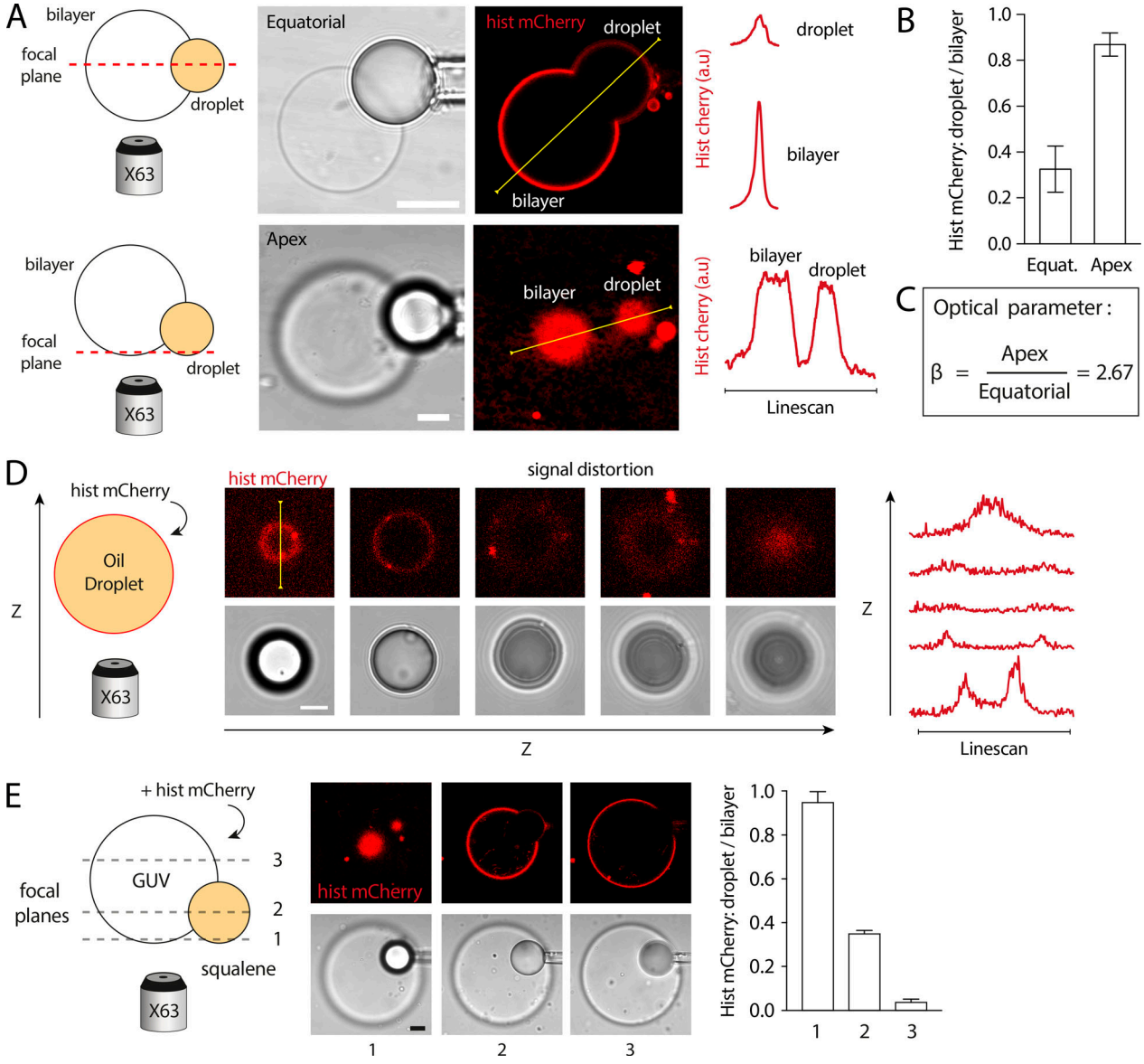

Figure S2. **Experimental determination of the optical correction factor (β) accounting for the optical index mismatch between the oil droplet and the external water phase, related to Materials and methods. (A)** DOPC:DGS-Ni-NTA (99:1) DEV embedding a TO aLD was tagged by histidine mCherry and observed at the equatorial cross section (up) and at its apex (bottom). Histidine mCherry fluorescence on the droplet and the bilayer was quantified at each cross-section. Scale bars, 5 µm. **(B)** Histidine mCherry fluorescence signal on the droplet normalized by signal on the bilayer quantified at each cross-section. Ratio at the equatorial cross-section shows significant attenuation (n > 15 DEVs quantified for each cross-section). **(C)** The correcting factor β is defined as the ratio of the signal at the apex of the droplet over the bilayer signal, divided by the droplet-bilayer signal ratio at the equatorial plane. The factor β was constant, equal to 2.67. **(D)** Left: TO droplet covered by a DOPC:DGS-Ni-NTA (99:1) PL mix was tagged by histidine mCherry and observed at different cross-sections. Right: Fluorescence signal was quantified, and revealed significant signal attenuation at the equatorial cross-section. Scale bar, 10 µm. **(E)** Left: DOPC:DGS-Ni-NTA (99:1) DEV embedding a SQ droplet was tagged by histidine mCherry and observed at different cross-sections. Right: Histidine mCherry fluorescence ratio between the droplet and the bilayer was quantified at each cross-section. Scale bar, 5 µm.

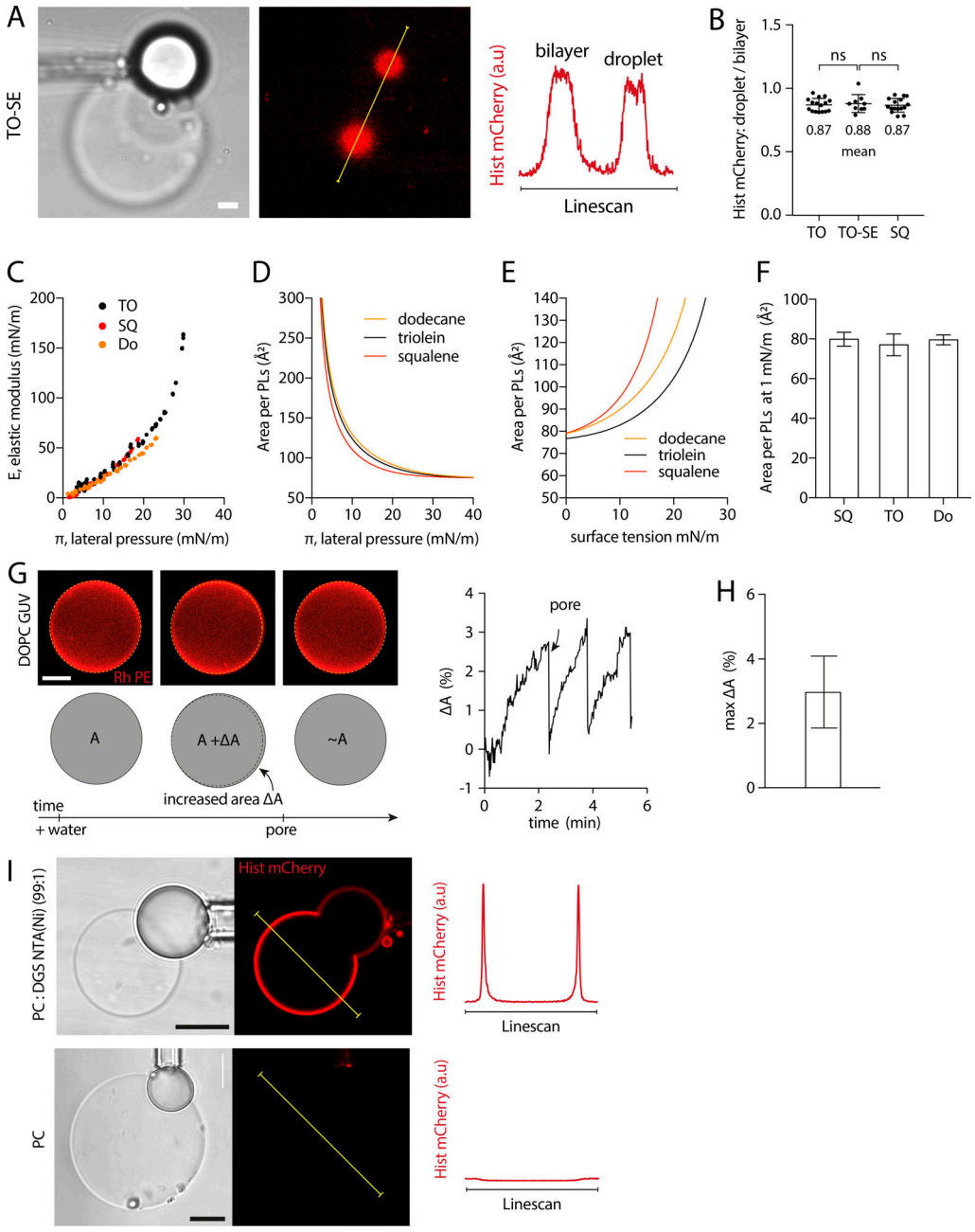

Figure S3. **Additional experimental determination of the PL density in DEV by using tagged PLs and the pending droplet experiment, related to Fig. 2. (A)** Representative confocal fluorescence images of mCherry-histidine marking PLs of a DEV containing TO-SE (3:1) aLDs. Linescans allow for quantification of fluorescence intensity on the bilayer and droplet surface. Scale bar, 5 µm. **(B)** Quantification of the ratio between the droplet and bilayer fluorescence intensity for TO, TO-SE, and SQ aLDs. *t* test shows no significant difference. Data are represented as mean ± SD. Related to Fig. 2, B and C. **(C)** PC-covered oil droplets were characterized using the pending droplet experiment. Resulting elastic modulus-lateral pressure (E-π) isotherms for SQ and TO and dodecane oil phases. See Fig. S4, A–C, for full data. Related to Fig. 2, D and E. **(D)** Area per PC molecule as a function of lateral pressure for SQ, dodecane, and TO oils; data obtained by fitting experimental E-π isotherms with a Frumkin theoretical model. See Fig. S4, A–C, for supporting data. Related to Fig. 2 F. **(E)** Area per PC molecule as a function of droplet surface tension for SQ, dodecane, and TO oils. Surface tension is obtained by subtracting the lateral pressure to bare oil buffer surface tension. Related to Fig. 2 G. **(F)** Area per PC molecule on SQ, dodecane, and TO droplets, at 1 mN/m surface tension. Surface tension of 1 mN/m was chosen as the average surface tension of aLDs in DEV. Related to Fig. 2 G. **(G)** Left: MQ water is added to the surrounding medium of a GUV (PC tagged with 1% Rhodamine-DOPE). The GUV swells because of the osmotic pressure imbalance, increasing its surface area by ΔA. The resulting increase of surface tension favors pore formation in the membrane. When a pore is formed, the internal solution is ejected and the GUV deflates, reducing both surface tension and surface area. At low tension, the pore is able to close, and the phenomenon can start again, resulting in a series of inflations-deflations of the GUV. Right: Quantification of GUV area variation (ΔA) after water addition to the external medium at time = 0 s. Arrows indicate an event of pore formation resulting in a quick decrease of ΔA. **(H)** Quantification of the GUV area variation before the pore formation (max ΔA), corresponding to the maximum area increase that the GUV membrane can endure. The average was found around 3% (GUV composition: PC 99%, rhodamine-DOPE 1%; data of 5 GUVs). **(I)** PC DEVs presenting TO aLDs were produced with and without DGS-Ni-NTA. After being incubated for 10 min with mCherry-histidine, DEV were imaged; mCherry-histidine was recruited only on DEV supplemented with DGS-Ni-NTA; see linescans on the left. Scale bars, 10 µm.

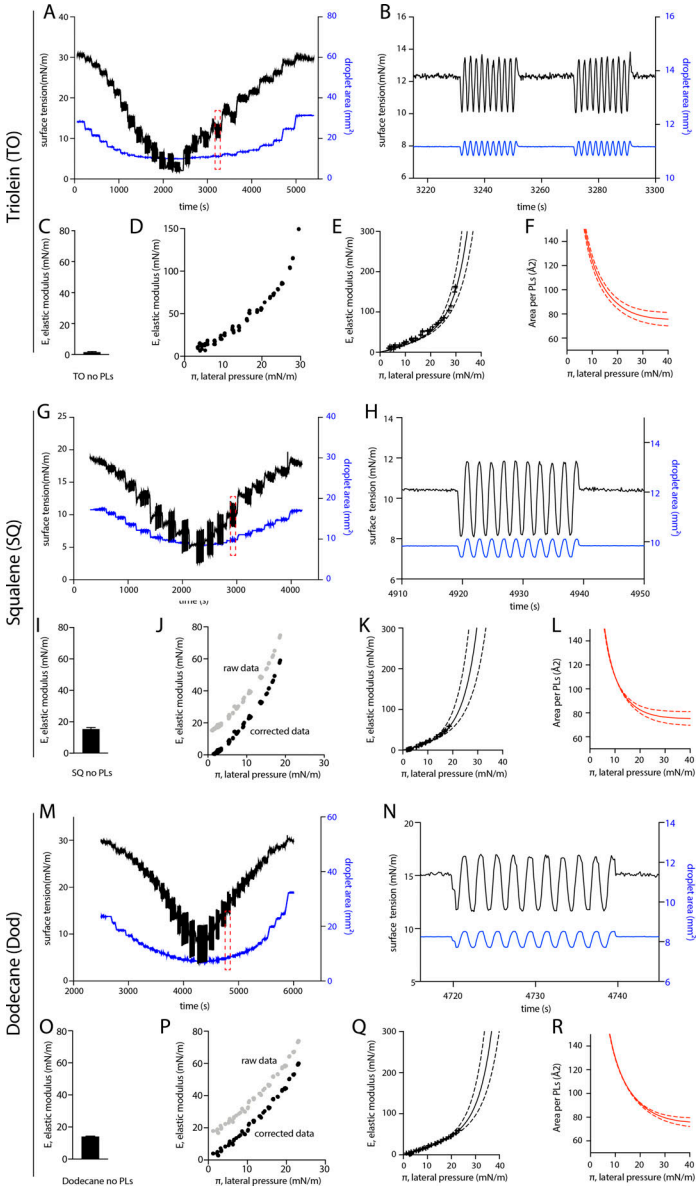

Figure S4. **Pending droplet experimental raw data used for the determination of the area per PL as a function of the lateral pressure, related to Fig. 2. (A)** Area and tension variation of a representative droplet tensiometer experiment using a TO droplet covered by DOPC PL (referred to below as PC). The droplet surface area was decreased and increased, and its surface tension was concomitantly measured. **(B)** Zoom-in: Sinusoidal area oscillations and resulting surface tension variation. Elastic modulus of the interface was calculated by the spectral analysis of the area oscillations and surface tension. **(C)** Elastic modulus (E) of bare TO-buffer interface. **(D)** The resulting elastic modulus against the lateral pressure (E-π) isotherm for TO oil covered by PC, determined from data presented in A. The lateral pressure (π) is calculated as the bare oil-buffer surface tension (s_0) minus the measured oil-PL-buffer surface tension (s): ($\pi = s_0$-s). **(E)** The E-π curve is fitted by a Frumkin theoretical isotherm. Dashed lines show error range on data fitting. **(F)** The resulting area per PC molecule as a function of the lateral pressure (π) on TO oil droplet, obtained by the Frumkin fitting model. **(G)** Area and tension variation of a representative droplet tensiometer experiment using a SQ droplet covered by DOPC PL (referred to below as PC). The droplet surface area was decreased and increased, and its surface tension was concomitantly measured. **(H)** Zoom-in: Sinusoidal area oscillations and resulting surface tension variation. Elastic modulus of the interface was calculated by the spectral analysis of the area oscillations and surface tension. **(I)** Elastic modulus (E) of bare SQ-buffer interface. **(J)** The resulting elastic modulus against the lateral pressure (E-π) isotherm for SQ oil covered by PC, determined from data presented in G. The lateral pressure (π) is calculated as the bare oil-buffer surface tension (s_0) minus the measured oil-PL-buffer surface tension (s): ($\pi = s_0$-s). **(K)** The E-π curve is fitted by a Frumkin theoretical isotherm. Dashed lines show error range on data fitting. **(L)** The resulting area per PC molecule as a function of the lateral pressure (π) on SQ oil droplet, obtained by the Frumkin fitting model. **(M)** Area and tension variation of a representative droplet tensiometer experiment using a dodecane droplet covered by DOPC PL (referred to below as PC). The droplet surface area was decreased and increased, and its surface tension was concomitantly measured. **(N)** Zoom-in: Sinusoidal area oscillations and resulting surface tension variation. Elastic modulus of the interface was calculated by the spectral analysis of the area oscillations and surface tension. **(O)** Elastic modulus (E) of bare dodecane-buffer interface. **(P)** The resulting elastic modulus against the lateral pressure (E-π) isotherm for dodecane oil covered by PC, determined from data presented in M. The lateral pressure (π) is calculated as the bare oil-buffer surface tension (s_0) minus the measured oil-PL-buffer surface tension (s): ($\pi = s_0$-s). **(Q)** The E-π curve is fitted by a Frumkin theoretical isotherm. Dashed lines show error range on data fitting. **(R)** The resulting area per PC molecule as a function of the lateral pressure (π) on dodecane oil droplet, obtained by the Frumkin fitting model.

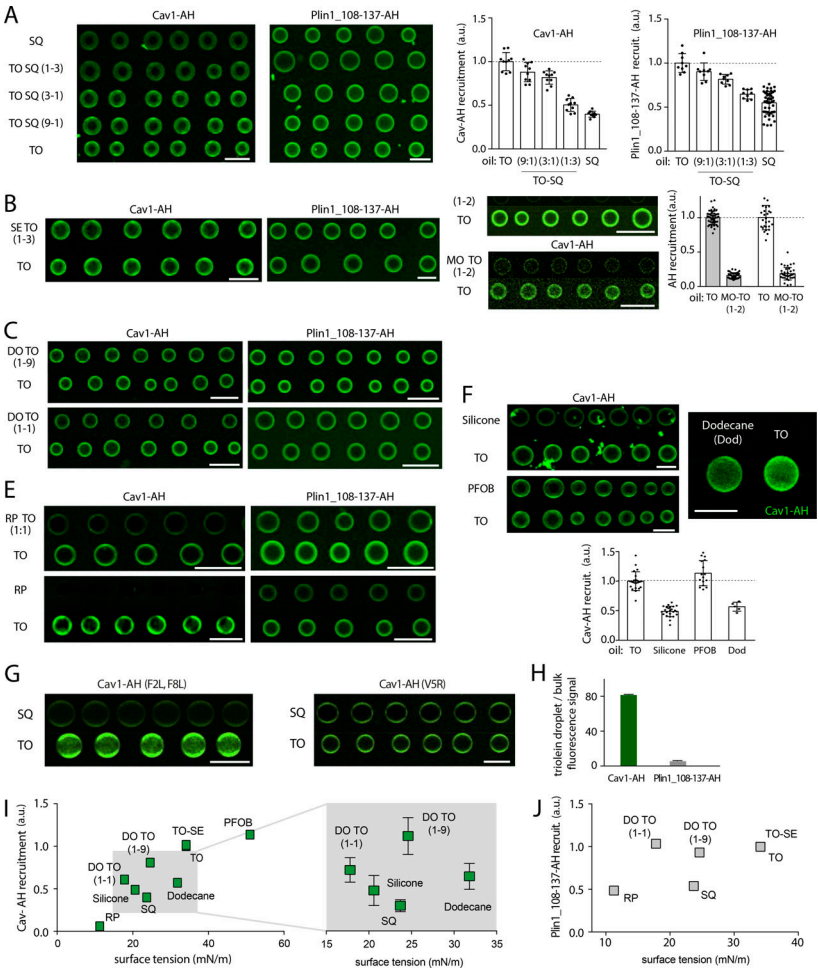

Figure S5. **Confocal micrographs corresponding to the quantification of recruitment of AHs to bare droplets of various oil compositions, related to Fig. 3. (A)** Left: PL-free SQ and TO, and mixtures thereof, TO-SQ (TO/SQ 1/9, 1/3, 3/1), are made in buffer containing Cav1-AH or Plin1_108-137-AH. Representative confocal fluorescence images showing the recruitment level of AHs are shown. The surface fluorescent signal is quantified on each droplet. Scale bar, 50 µm. Right: Corresponding quantification of the fluorescence intensity of Cav1-AH and Plin1_108-137-AH at the surface of droplets of SQ, and TO-SQ mixtures, normalized by the fluorescence intensity on TO droplets. Data are represented as mean ± SD. For Cav1-AH, *t* test shows significant differences between TO and TO/SQ (9/1), TO and TO/SQ (3/1), TO and TO/SQ (1/3), TO and SQ, with the respective P values P = 0.014, P = 0.0005, P < 0.0001, and P < 0.0001. For Plin1_108-137-AH, the *t* test shows no significant differences between TO and TO/SQ (9/1) but shows significant differences between TO and TO/SQ (3/1), TO and TO/SQ (1/3), TO and SQ, with the respective P values P = 0.063, P = 0.0003, P < 0.0001, and P < 0.0001. **(B)** PL-free SE-TO (SE/TO, 1/3) and TO are formed in buffer containing Cav1-AH or Plin1_108-137-AH. Representative confocal fluorescence images showing the recruitment level of AHs are presented. The surface fluorescent signal is quantified on each droplet. Scale bar, 50 µm. Related to Fig. 3 C. **(C)** PL-free droplets containing TO or diolein-TO mixtures (DO/TO, 1/9, 1/1, vol/vol) are formed in buffer in the presence of Cav1-AH or Plin1_108-137-AH. Representative confocal fluorescence images showing the recruitment level of AHs are presented. The surface fluorescent signal is quantified on each droplet. Scale bar, 50 µm. Related to Fig. 3 C. **(D)** Left: PL-free droplets of TO or monolein-TO mixture (MO-TO, 1/2, vol/vol) are formed in buffer containing AHs Cav1-AH or Plin1_108-137-AH. Representative confocal fluorescence images showing the recruitment level of AHs are presented. The surface fluorescent signal is quantified on each droplet. Scale bar, 50 µm. Right: Corresponding quantification of the fluorescence intensity of Cav1-AH and Plin1_108-137-AH at the surface of monolein-TO (1/2) and TO droplets, normalized by the fluorescence intensity of the TO droplet. *t* test shows significant differences between TO and MO-TO (1/2), for both Cav1-AH and Plin1(108–137)-AH (P < 0.0001). Data are represented as mean ± SD. **(E)** PL-free droplets of TO or RP/TO (1/1) are formed in buffer containing Cav1-AH or Plin1_108-137-AH. Representative confocal fluorescence images showing the recruitment level of AHs are presented. The surface fluorescent signal is quantified on each droplet. Scale bar, 50 µm. Related to Fig. 3 C. **(F)** Top: PL-free droplets of TO, silicone, perfluorooctylbromide (PFOB), or dodecane (Dod) are formed in buffer containing Cav1-AH. Representative confocal fluorescence images showing the recruitment level of AHs are presented. The surface fluorescent signal is quantified on each droplet. Scale bar, 50 µm. Bottom: Corresponding quantification of the fluorescence intensity of Cav1-AH and Plin1_108-137-AH at the surface of silicone, PFOB, Dod, and TO droplets, normalized by the fluorescence intensity on TO droplets. *t* test shows significant differences between TO and silicone oil, TO and PFOB, and TO and dodecane, with P values: P < 0.0001, P = 0.03, and P < 0.0001, respectively. Data are represented as mean ± SD. **(G)** PL-free droplets of SQ or TO droplets are formed in buffer containing Cav1-AH, Cav1-AH(F2L,F8L), or Cav1-AH(V5R). Representative confocal fluorescence images showing the recruitment level of these AHs are presented. The surface fluorescent signal is quantified on each droplet. Scale bar, 50 µm. Related to Fig. 3 D. **(H)** Net binding of Cav1-AH and Plin1_107-138-AH to bare TO-buffer interface. Quantification was done by determining the signal on the droplet divided by the signal in the bulk. **(I)** Cav1-AH recruitment to various PL-free oil droplets as a function of the oil-buffer surface tension. Cav1-AH recruitment values are normalized by the AH recruitment on TO droplets. The inset showcases data where there is no correlation between the surface tension and Cav1-AH recruitment level. **(J)** Plin1_108-137-AH recruitment to various PL-free oil droplets as a function of the oil-buffer surface tension. Plin1_108-137 recruitment values are normalized by the AH recruitment on TO droplets.

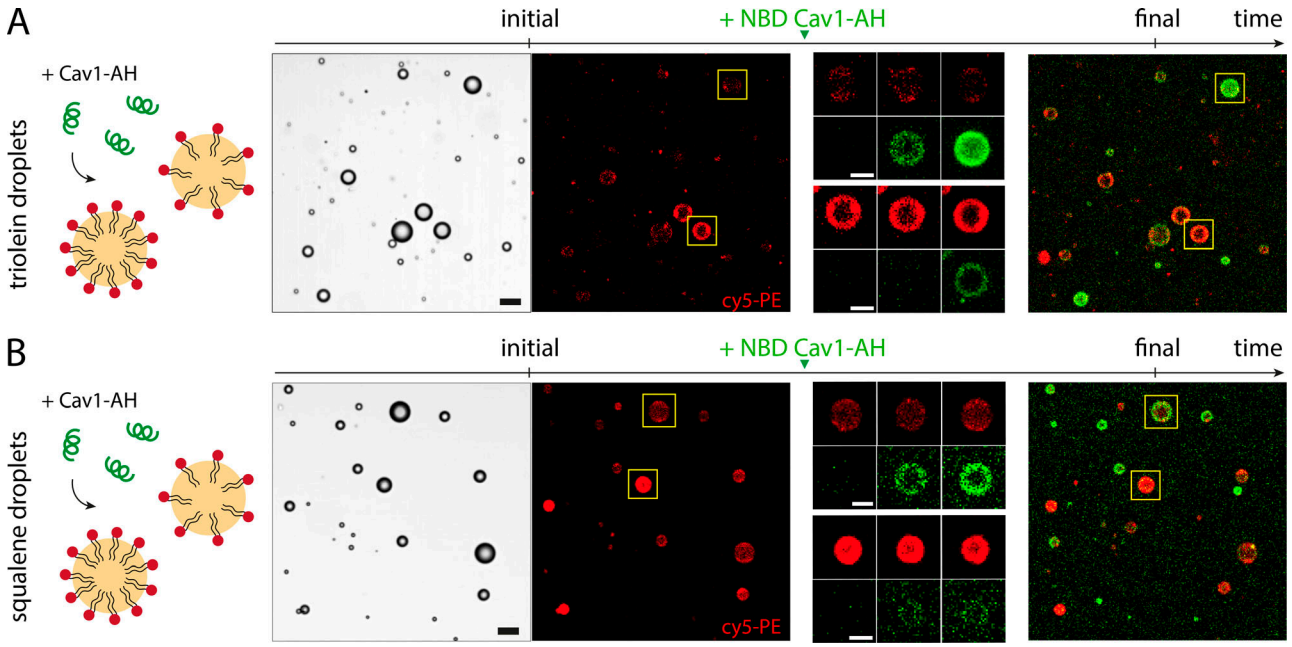

Figure S6. **Recruitment time-lapse of Cav1-AH to TO and SQ droplets of various PL densities, related to Fig. 4. (A)** TO aLD with heterogeneous PL densities (DOPC:Cy5-DOPE; 99:1) were prepared in a buffer solution (see Cy5-DOPE channel) and observed by confocal microscopy. NBD-tagged Cav1-AH was added to the bulk solution and recruitment observed over time on droplets presenting high and low PL density (see selected droplets depicted by yellow squares). After 20 min, droplets presenting the lower PL density had the higher NBD-tagged Cav1-AH signal (right merge image). Scale bar, 20 µm, and 10 µm for insets. Related to Fig. 4 B. **(B)** SQ aLD with heterogeneous PL densities (DOPC:Cy5-DOPE; 99:1) were prepared in a buffer solution (see Cy5-DOPE channel) and observed by confocal microscopy. NBD-tagged Cav1-AH was added to the bulk solution and recruitment observed over time on droplets presenting high and low PL density (see selected droplets depicted by yellow squares). After 20 min, droplets presenting the lower PL density presented the higher NBD-tagged Cav1-AH signal (right merge image). Note the weaker Cav1-AH signal on droplets as compared with TO droplets of Fig. S5 A. Microscope settings were identical in all Fig. S5 A experiments. Scale bars, 20 µm, and 10 µm for insets. Related to Fig. 4 C.